OXFORD

Journal of Petrology, 2024, **65**, egae050
https://doi.org/10.1093/petrology/egae050
ADVANCE ACCESS PUBLICATION DATE 18 MAY 2024
Original Manuscript

To Mix or Not to Mix: Details of Magma Storage, Recharge, and Remobilization during the Pacheco Stage at Misti Volcano, Peru (≤21–2 ka)

MARIE K. TAKACH [1,2,*], FRANK J. TEPLEY III[1], CHRISTOPHER J. HARPEL[3], RIGOBERTO AGUILAR[4] and MARCO RIVERA[5]

[1]College of Earth, Ocean, and Atmospheric Sciences, Oregon State University, 101 SW 26th St, Corvallis, Oregon 97331, USA
[2]Department of Geological Sciences, Central Washington University, 400 E University Way, Ellensburg, Washington 98926, USA
[3]U.S. Geological Survey, Volcano Disaster Assistance Program, Cascades Volcano Observatory, 1300 SE Cardinal Court, Suite 100, Vancouver, Washington 98683, USA
[4]Instituto Geológico, Minero y Metalúrgico, Dirección de Geología Ambiental y Riesgo Geológico, Calle Sevilla 127, Cayma, Arequipa, Perú
[5]eInstituto Geofísico del Perú, Observatorio Vulcanológico del Sur, Asentamiento Humano José María Arguedas, Mz D, Lt 8, Sachaca, Arequipa, Perú

*Corresponding author: E-mail: marie.takach@gmail.com

We investigate ten of the most recent tephra-fall deposits emplaced between ≤21 and 2 ka from the Pacheco stage of Misti volcano, Peru, to elucidate magma dynamics and explosive eruption triggers related to magma storage, recharge, and remobilization. Whole-rock, glass, and mineral textures and compositions indicate the presence of broadly felsic, intermediate, and mafic magmas in a chemically and thermally stratified magma storage system (Zones 1–3) that interact to differing extents prior to eruption. Intermediate magmas are defined by plagioclase + amphibole + two-pyroxenes + Fe-Ti oxides and phase equilibria indicate they formed at ∼300 to 600 MPa and ∼950°C to 1000°C. Intermediate magmas dominate the Pacheco stage and either erupted alone as hybridized magmas or mingled with minor volumes of cool felsic magmas (∼800°C) in which only plagioclase + Fe-Ti oxides are stable. Felsic magmas do not exclusively comprise any tephra-fall deposit emplaced during the Pacheco stage but were remobilized by recharge and mixing with intermediate magmas in order to erupt. Furthermore, felsic-hosted amphibole cognate to the intermediate magmas are reacted despite the felsic magmas being water saturated, which suggests they are staged above the amphibole stability limit (≤200 MPa). The cryptic presence of mafic magmas is indicated by high-An plagioclase cores ($An_{74–88}$), rare anhedral olivine ($Fo_{77–80}$), and possibly high Mg# augite and amphibole (up to Mg# 84 and 77, respectively). The dearth of basalt to basaltic andesite melts recorded in erupted glasses and exclusivity of high-An plagioclase to crystal cores signals mafic magmas are staged deeper in the crust than the intermediate magmas. Periodic interactions between these magmas tracked via glass compositions and crystal exchange reveal an alternation between the production of mingled magmas and their eruption shortly after a recharge event, followed by a period of homogenization and eruption of hybridized magmas. As such, we identify magma recharge as a key mechanism by which half of the explosive eruptions were triggered in the Pacheco stage. A >100°C increase in Misti's fumarole temperatures from 1967 to 2018 coincident with changes in fumarolic gas compositions is consistent with degassing of a mafic recharge magma, signaling that Misti could produce similar explosive eruptions in the future.

Key words: Arequipa; Peru; magma mixing; magma recharge; magma storage; Misti volcano; thermobarometry

INTRODUCTION

Petrological investigations characterizing an individual volcano include probing its eruptive products for insight into its magma genesis, magma storage system, and eruption triggers. El Misti volcano (hereafter referred to as Misti) in southern Peru (Fig. 1) is targeted here because (1) recent work delineates ten VEI 2–5 eruptions via documentation of tephra-fall deposits emplaced during the Pacheco stage (≤21–2 ka) (Cacya *et al.*, 2007; Harpel *et al.*, 2018, 2021), allowing for investigation of a stratigraphically controlled consecutive sequence of young explosive eruptions, and (2) Misti poses significant threats to Arequipa, Peru's second largest city (population > 1.1 million; INEI, 2018) centered <18 km from the summit. Misti's volcaniclastic deposits form a ∼200-km^2 volcaniclastic fan on which Arequipa developed (Legros, 2001; Thouret *et al.*, 2001). Arequipa has essential infrastructure in high volcanic hazard zones such as the Aguada Blanca dam and hydroelectric complex (Fig. 2), which is connected to the national energy grid and stores critical water supplies in an otherwise arid region (Mariño *et al.*, 2007, 2016). These risks make it critical to understand the petrology of Misti's young deposits.

Existing examinations provide a crucial synopsis of Misti's entire eruptive history and petrogenesis (Legros, 1998, 2001; Thouret *et al.*, 2001; Ruprecht & Wörner, 2007; Rivera *et al.*, 2017), but only Misti's Plinian ca. 2-ka, Sacarosa, and Autopista eruptions are described in great detail (Thouret *et al.*, 2001; Cacya *et al.*, 2007; Harpel *et al.*, 2011, 2023; Cobeñas *et al.*, 2012; Tepley III *et al.*, 2013; Cuno, 2018). There remains a gap in comprehending magma petrogenesis and processes driving eruptive activity for much of Misti's history.

The Pacheco stage represents magmas in which we find abundant evidence for the processes of magma recharge and rejuvenation. We use the definition of recharge as the addition of

RECEIVED: MAY 3, 2023; **REVISED:** APRIL 29, 2024; **ACCEPTED:** MAY 13, 2024

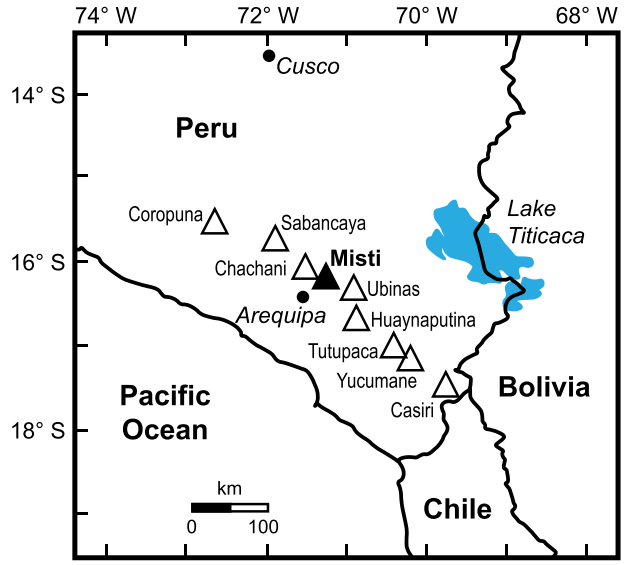

Fig. 1. Locations of southern Peru's active and potentially active volcanoes (triangles) after de Silva & Francis (1991). Note Misti volcano's location near Arequipa, the second largest city in Peru. Large bold text indicates countries and oceans, italic text shows major cities and lakes, and solid black lines mark country borders.

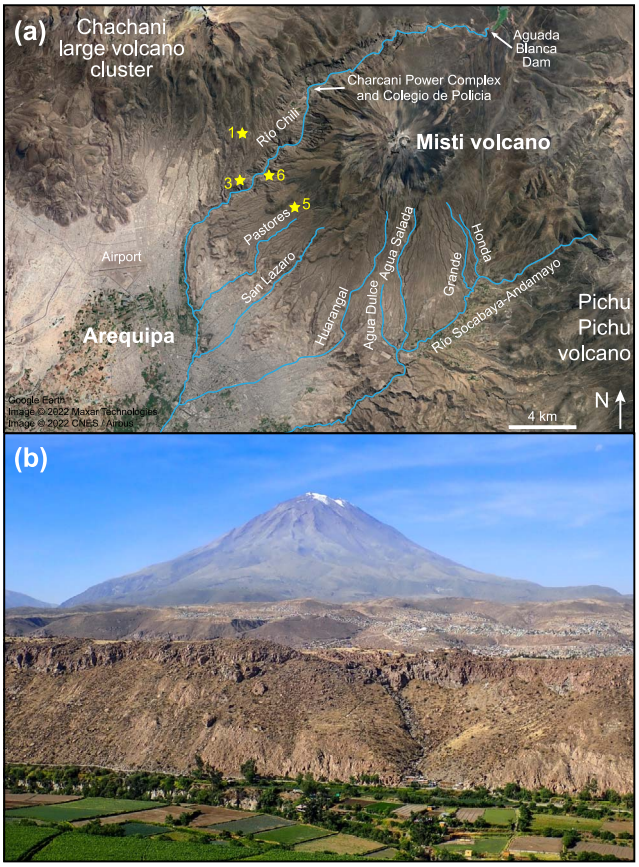

Fig. 2. (a) Misti volcano and the surrounding region highlighting major drainages and locations mentioned in the text, after Harpel *et al.* (2011). Stars represent sites mentioned in Fig. 3. Coordinates of all sites are found in Electronic Appendix 1. Site 1 approximates the location of a roadcut with a complete section of Pacheco stage deposits. (b) Photograph looking northeast toward Misti volcano from the west side of the Río Chili, ~15 km from the volcano's summit. The Río Chili is downstream of the Aguada Blanca dam and hosts the Charcani power complex in a high volcanic hazard zone (Mariño *et al.*, 2016). Also in the midground of (b) are extensive human developments in moderate-high hazard zones.

relatively mafic magma to a resident felsic magma, and magma rejuvenation as the addition of a magma broadly similar in composition to the resident magma (Kent *et al.*, 2023). Regardless of compositions involved, these processes lead to magma mixing, which describes general interactions between two different magmas without implying the state of the final product (Wilcox, 1999). Magma mixing is divided into: (1) mingling, which occurs when viscosity contrasts between recharge and resident magmas are large and mechanical mixing is initially favored, leaving behind textural evidence at the hand sample scale and forming bimodal magmas, and (2) hybridization, which occurs when viscosity contrasts between magmas are low and homogenization is driven by diffusion across geochemical gradients (Bacon, 1986). Exclusively mingled magmas are rare in nature (Morgavi *et al.*, 2022) including at Misti, where bimodal magmas contain crystals with evidence of previous mixing events. Here, we use the term mingled when bimodal glass compositions are present in a unit. For rejuvenation by similar magmas in which the largest differences are temperature or volatile content, or hybridization of once bimodal melts, mixing is recorded in surviving crystal cargo (e.g. Clynne, 1999; Tepley *et al.*, 2000; Armienti *et al.*, 2007; Ruprecht & Wörner, 2007). Finally, we recognize that some chemical variability can be attributed to eruption from a zoned magma chamber (e.g. Hildreth, 1981; Matthews *et al.*, 1999).

Per these definitions, we present textural and geochemical evidence of mingled and hybridized magmas from repeating magma recharge or rejuvenation events followed by mixing and eruption at Misti. While eruption of individual dacitic and rhyolitic magmas ceased just prior to the Pacheco stage (e.g. Legros, 2001; Harpel *et al.*, 2023), Pacheco stage explosive eruptions sample felsic magmas as one mixing component. We also introduce temperatures and pressures estimated via thermobarometry and combine them with textures and compositions to delineate details of Misti's petrology from ≤21–2 ka. Although Misti produced effusive eruptions during this time (Thouret *et al.*, 2001; Ruprecht & Wörner, 2007), it is unclear where they fit into Pacheco stage stratigraphy and conclusions drawn herein are based only on explosive eruptive deposits.

These ten eruptive deposits provide an exceptional opportunity to probe the commonly cited eruption triggers of mafic recharge and rejuvenation (e.g. Sparks *et al.*, 1977; Clynne, 1999; de Silva *et al.*, 2008; Ferlito *et al.*, 2009; Kent *et al.*, 2023). Results from this study, particularly those regarding eruption triggers, can help scientists interpret volcano monitoring data, inform eruption forecasts, and thereby mitigate impacts on Arequipa. Documentation of single eruptions with VEI ≥5 in the Central Volcanic Zone (CVZ) of the Andes is sparse (Siebert *et al.*, 2011; Harpel *et al.*, 2023), and magma mixing is documented in nearby active volcanoes (e.g. Nevado Sabancaya, Gerbe & Thouret, 2004; Rivera *et al.*, 2023; Ubinas volcano, Rivera *et al.*, 2014), so deductions from this study can also be used to gain a broader understanding of explosive activity in the CVZ and similar arc volcanoes worldwide.

GEOLOGICAL BACKGROUND

Overview of eruptive history

Misti is a relatively young (≥112 ka) stratovolcano in the CVZ (de Silva & Francis, 1991) that has mostly erupted andesites-dacites with minor rhyolites emplaced as lava flows, domes, pyroclastic density current (PDC) deposits, and tephra-fall deposits. Misti

produced ≥24 explosive eruptions with VEI 2–5 since ~45 ka whose products fall into three lithological groups: (1) mica-bearing rhyolites, (2) mica-bearing dacites, and (3) two-pyroxene and amphibole-bearing andesites (Legros, 1998, 2001; Thouret *et al.*, 2001; Ruprecht & Wörner, 2007; Rivera *et al.*, 2017; Harpel *et al.*, 2018, 2021, 2023; Takach *et al.*, 2021, 2022). Misti's Plinian VEI 5 eruption at ca. 2 ka emplaced voluminous tephra-fall deposits, PDC deposits, and lahars which underlie Arequipa (Thouret *et al.*, 1995, 1999, 2001; Legros, 1998, 2001; Harpel *et al.*, 2011; Cobeñas *et al.*, 2012). This marks the most recent eruption in the Pacheco stage (Fig. 3), which contains at least three VEI 5 eruptions (Harpel *et al.*, 2018, 2021, 2023). Historically, Misti produced several VEI 1 phreatic or phreatomagmatic eruptions and periods of heightened fumarolic activity as recently as 1985. Prior to the early nineteenth century, a small dome was extruded into the crater of a summit cinder cone. This cone formed during a small-volume explosive eruption in the mid-fifteenth century, which disbursed ash and impacted the local indigenous people (Hantke & Parodi, 1966; Chávez Chávez, 1992; Thouret *et al.*, 2001; Ruprecht & Wörner, 2007). Misti is fumarolic and monitored daily by permanent seismic stations and periodic fumarole measurements (Birnie & Hall, 1974; Moussallam *et al.*, 2017; Vlastelic *et al.*, 2022).

Tephrostratigraphy

Pacheco stage tephra-fall deposits are dispersed to the west-southwest of Misti toward Arequipa. A complete section is exposed west of Misti on the southeast flank of Chachani large volcanic cluster (Fig. 2a). In this paper, deposits we recognize as mingled or hybridized are identified in bold and italic font, respectively. Autopista (*A*) (≤21 ka; Cacya *et al.*, 2007) is the oldest unit in the sequence deposited atop an unconformity, followed by Ponche Gris (**PG**), Ponche Iridescente (*PI*), Sandwich Inferior (**SI**), Sandwich Superior (**SS**), Sancayo (*S*), La Rosada (**LR**), Apo (*AP*), Misquirichi (**M**), and the ca. 2-ka deposit (**2K**) (Fig. 3). The unit, **2K**, is near the modern surface and often overlain by Huaynaputina's 1600 CE ash (Thouret *et al.*, 1999; Adams *et al.*, 2001) and sometimes a black tephra-fall deposit from Misti's fifteenth-century eruption (Legros, 2001). Units are separated by sandy paleosols and layers of reworked material of varying thicknesses (Electronic Appendix 1). Results here focus on *A* through **M** but published geochemical data from **2K** (Tepley III *et al.*, 2013) and new **2K** thermobarometry calculations are integrated for comparative purposes.

ANALYTICAL METHODS

Whole-rock geochemical analyses were conducted at Hamilton Analytical Laboratory on 16 samples from nine eruptive units using X-ray fluorescence (XRF) for major elements following methods of Johnson *et al.* (1999) and laser ablation-inductively coupled plasma-mass spectrometry (LA-ICP-MS) for trace elements following methods of Conrey *et al.* (2019) (Takach *et al.*, 2024; Electronic Appendix 2). Tephra types from each unit were identified based on macroscopic differences and glass geochemistry for whole-rock analyses. Small rock chips of each macroscopically distinct tephra were selected to avoid as much cross-contamination as possible.

We examined two to six thin sections per unit to petrographically and geochemically characterize represented magmas. Electron microprobe (EMP) analyses (Takach *et al.*, 2024; Electronic Appendices 3–5) and backscattered electron (BSE) images were collected on ~30 crystals of every phase when possible (excluding trace phases) at Oregon State University using a CAMECA SX-100. Relative standard deviation is typically <5% for major elements and <5–15% for minor or trace elements. We used these analyses in Thermobar (Wieser *et al.*, 2022) to calculate intensive parameters except for Fe-Ti oxide thermometry, for which we used the online geothermooxybarometer calculator of Ghiorso & Evans (2008) (https://melts.ofm-research.org/calcForms.html). Approximations of these parameters are given as averages of individual estimates, which significantly lowers associated uncertainty (e.g. Putirka, 2016). All uncertainties presented are the expected standard errors of estimation for a given method and are found in the original publications. Supplementary information on decisions made to calculate intensive parameters is found in Electronic Appendix 6.

Three units were also selected to collect plagioclase trace elements via LA-ICP-MS in Oregon State University's W.M. Keck Collaboratory for Plasma Spectrometry using an Applied Spectra RESOlution ArF Excimer laser system with a ThermoFisher Scientific iCAP-RQICP-MS (Electronic Appendices 4–5), gathered following the method of Lubbers *et al.* (2022) and reduced with LaserTRAM-DB (Lubbers *et al.*, 2021). Analyses indicate precision for trace element measurements is <5%. Further details on EMP and LA-ICP-MS analyses are described in Electronic Appendix 5.

PETROLOGY OF TEPHRA-FALL DEPOSITS

Due to the number of textural and petrologic datasets presented here, we present results for each phase followed directly by basic interpretations. These sections are then synthesized into a discussion of Misti's magmas and their storage system during the Pacheco stage.

Lithology, textures, and whole-rock geochemistry

Pacheco stage tephra-fall deposits include a variety of textures and compositions. In hand sample, color and texture suggest the existence of at least two distinct magmas. Except for *A*, dominant tephra is a light to dark brown scoria with minor light gray to white pumice (Fig. 3). *A* is composed of light gray-buff-pink tephra. Tephra from all deposits are porphyritic and contain plagioclase + two-pyroxenes + amphibole + Fe-Ti oxides with trace apatite. A single zoned Cr-spinel is identified in **SI**'s dark scoria. One olivine-bearing glomerocryst is hosted in *S*, and **PI** hosts seven subhedral to anhedral olivine ± clinopyroxene microlites. Scoria qualitatively constitutes an overwhelming proportion of the erupted volume (>98%) in these deposits and a light-colored pumice is rare (≤2%) in **PI**, **SI**, **SS**, **LR**, and **M**. Unit **2K** represents an outlier, as it contains a light-colored pumice in proportions up to a few tens of percent. Textural relationships in mingled deposits (Figs. 3–4) include discrete tephra from each magmatic product, banding, and mm- to μm-sized wisps and globules of one type within the other. Banded textures are common in **2K** but rare in remaining units. Contacts between mingled materials are typically irregular and sometimes diffuse, and light-colored tephra tend to have higher crystallinities than the dark-colored tephra, especially in **SI** and **SS**, whose white pumice contain abundant plagioclase and pyroxene microphenocrysts and microlites.

Whole-rock analyses from this study are plotted with data for eruptive products from Misti's entire history (Fig. 5; Legros, 2001; Ruprecht & Wörner, 2007; Rivera *et al.*, 2017), including **2K** mingled tephra from Tepley III *et al.* (2013). Most of Misti's eruptive products straddle the andesite-trachyandesite fields, with lesser dacite and rhyolite. Whole-rock samples from this study are also andesites-trachyandesites with one basaltic

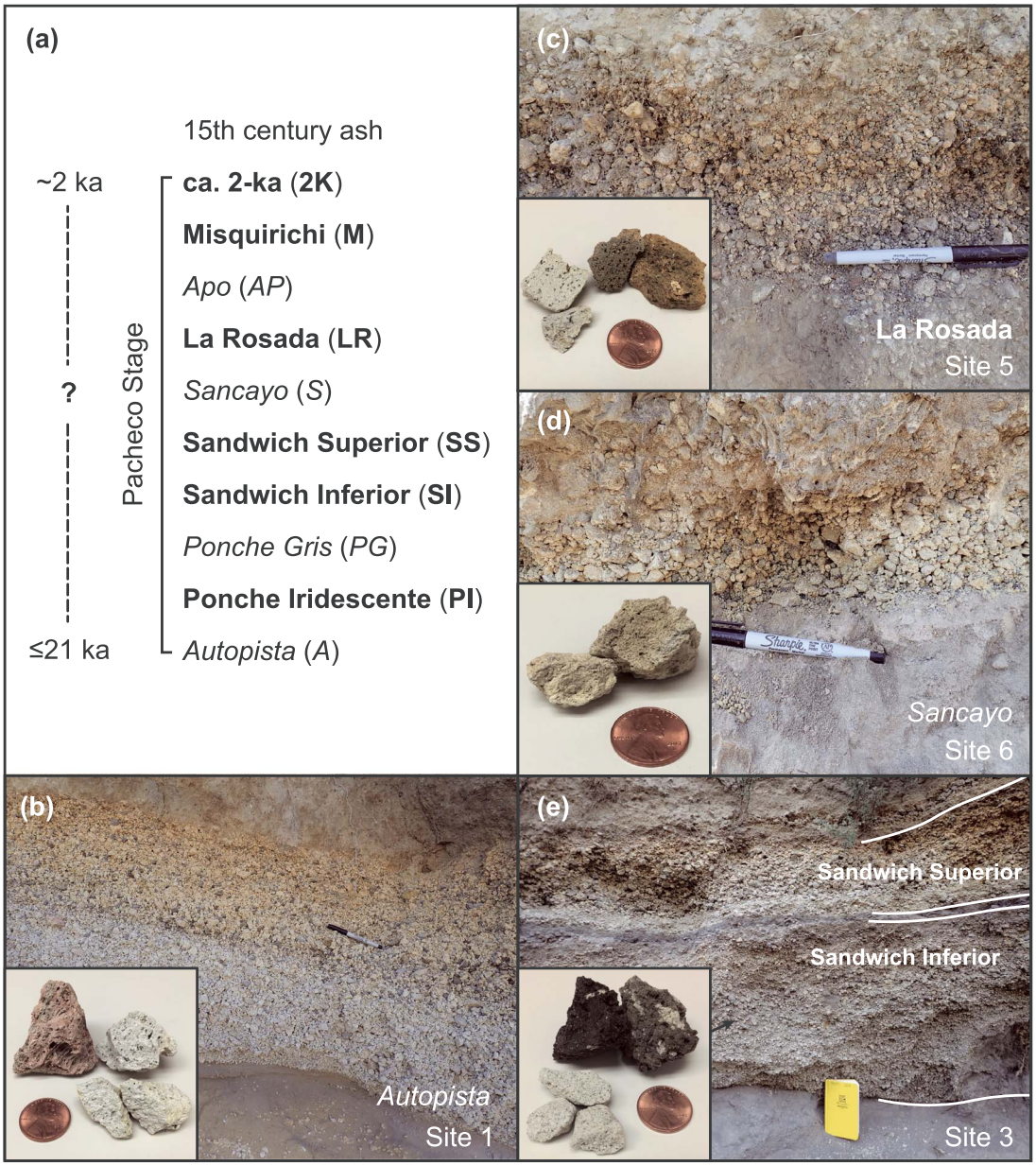

Fig. 3. Stratigraphic overview and photographs of some units in outcrop. Bold and italic text denote mingled and hybridized units, respectively, defined by glass compositions. (a) Schematic stratigraphic column highlighting Pacheco stage deposits and available age constraints (Legros, 1998, 2001; Thouret *et al.*, 1999, 2001; Cacya *et al.*, 2007; Harpel *et al.*, 2011). (b-e) Representative photographs of some Pacheco stage units taken at locations corresponding to starred sites in Fig. 2a. (b) Autopista is identified by a lithic-rich layer midway up the deposit, an orange hue defining the top half, and discrete pink pumice. (c) La Rosada has a consistent pink hue and light gray-white tephra that erupted discretely or with mingled textures, including rare banding. (d) Sancayo is a relatively thin gray pumice deposit. (e) Sandwich Inferior and Sandwich Superior are separated by a thin, gray layer of sand or reworked ash. Both deposits exhibit similar tephra, including discrete white pumice, dark brown scoria, and mingling textures. Inset photograph shows Sandwich Inferior tephra. Marker is 14-cm and notebook is 19-cm long.

andesite (*AP*). Whole-rock Mg# (=$(Mg/Fe+Mg)_{atomic}*100$) ranges from 45–52. With the exception of **2K** magmas, macroscopically distinct tephra from mingled eruptions, even those with high glass SiO_2 (wt.%) contents (e.g. **LR** and **SI**), have whole-rock compositions that span a narrow range of SiO_2 (wt.%). We suspect this is related to imperfect physical separation of magma types due to heterogeneities commonly seen in thin section and/or observed crystal fractions. Whereas less evolved melts in mingled deposits host low crystal fractions (e.g. ~5% in **SI** scoria), their relatively felsic melts host notably higher crystal fractions (e.g. up to ~20% in **SI** pumice). Since whole-rock analyses combine crystal and glass compositions, disparities in crystal fractions can partially account for the narrow range of observed SiO_2 (wt.%). Furthermore, units such as **SS** and **LR** show mm- to μm-sized mixing heterogeneities, partial hybridization in glass chemistry, and inferred crystal exchange (discussed below), which further complicates physical separation of magma types and leads to averaging of compositions in whole-rock analyses.

Glass geochemistry

Despite overlapping whole-rock compositions, we identify distinct magma types in each eruption dominantly based on glass compositions, using color, textures, and phase assemblages as

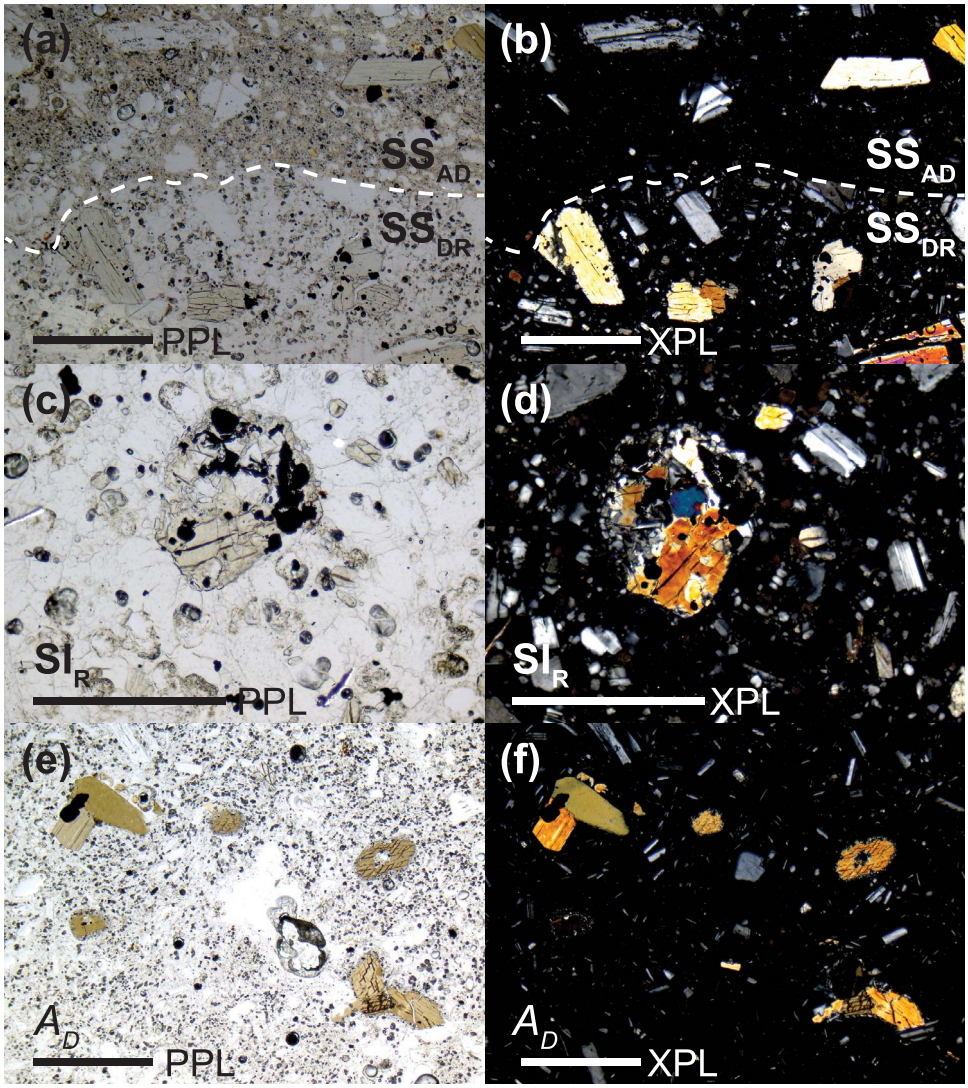

Fig. 4. Photomicrographs of Pacheco stage tephra. (a-b) Irregular contact (dashed line) between Sandwich Superior's intermediate (**SS_{AD}**) and felsic (**SS_{DR}**) glass. Note the relatively high abundance of plagioclase and pyroxene microlites in **SS_{DR}** compared to **SS_{AD}**. (c-d) Sandwich inferior's felsic (**SI_R**)-hosted clinopyroxene + orthopyroxene + Fe-Ti oxide glomerocryst with disequilibrium textures. Note fine-grained rim mantling the central crystal cluster. (e-f) Autopista example (A_D) highlighting coexistence of amphibole populations with and without reaction rims. Scale bars represent 100 μm. XPL, cross-polarized light; PPL, plane-polarized light; A, andesite-trachyandesite; D, dacite-trachydacite; R, rhyolite.

supporting information. These include (Fig. 5): A_D, **PI_A**, **PI_D**, PG_A, **SI_A**, **SI_R**, **SS_{AD}**, **SS_{DR}**, S_D, **LR_{AD}**, **LR_R**, AP_{AD}, **M_{R1}**, **M_{R2}**, **$2K_D$**, **$2K_R$**, where glass compositions in subscript are A, andesitic-trachyandesitic; D, dacitic-trachydacitic; and R, rhyolitic. Where glass compositions span multiple compositional fields, a range is used (e.g. **SS_{AD}**) and compositions are numbered when a bimodal unit's glasses exist in a single field (**M_{R1}** and **M_{R2}**).

Approximately 300 spots were measured on glasses from A through **M** (Figs. 5–6; Table 1). Lighter and darker colored tephra in a unit generally correlate to more and less silicic glass compositions, respectively. Glasses range from 60–78 wt.% SiO_2 and **PI**, **SI**, **SS**, **LR**, **M**, and **2K** are bimodal in glass compositions. These results agree well with the presence of both brown scoria and gray-white pumice in hand samples from these units. Most units have glass compositions between 60 and 67 wt.% SiO_2, and glasses with SiO_2 >72 wt.% solely represent the more silicic melts of bimodal eruptions. That is, magmas with the most silicic glasses have not fed discrete eruptions and are only found mingled with less silicic magmas. Bimodal magmas have varied amounts of separation in SiO_2 space. For example, **SI_A** and **SI_R** are separated by ~10 wt.% SiO_2 whereas **PI_A** and **PI_D** are separated by just ~3 wt.% SiO_2. Deposits in this sequence also display a range of compositions that indicate more than two discrete magma bodies are involved or there is substantial variability of magmas tapped within a chamber. Lastly, Fig. 7b plots glass SiO_2 (wt.%) in stratigraphic order, revealing a temporal alternation between hybridized and mingled deposits (e.g. A-**PI**-*PG*-**SI**).

We briefly investigate fractional crystallization (FC) as a mechanism to explain the diversity of magmas erupted during the Pacheco stage with Magma Chamber Simulator (MCS) (Bohrson *et al.*, 2014, 2020). We used the FC-only mode of MCS with rhyolite-MELTS version 1.1.0 (Ghiorso & Sack, 1995; Asimow & Ghiorso, 1998; Ghiorso *et al.*, 2002; Gualda *et al.*, 2012; Ghiorso & Gualda, 2015). The least silicic glass composition in our dataset (PG_A) is the initial composition fractionally crystallized at 200, 400, and 600 MPa. Modeled phase assemblages match those observed best at 400 and 600 MPa and temperature steps above 800–900°C (Fig. 6), which are consistent with estimated temperatures and

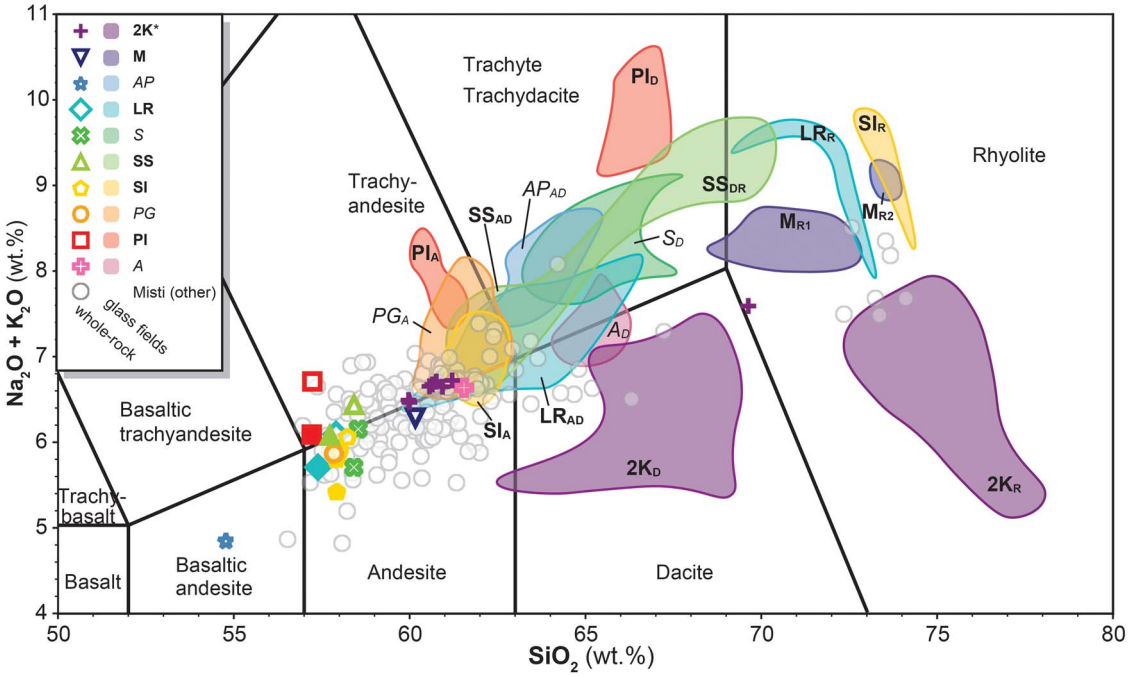

Fig. 5. Total-alkali silica diagram (after LeBas *et al.*, 1986) showing whole-rock and glass compositions (normalized to 100%) of Pacheco stage deposits. Shaded fields represent glass analyses collected by electron microprobe and symbols show whole-rock data collected via x-ray fluorescence. Filled symbols represent light-colored pumice when present in a unit in addition to brown scoria. Pumice generally contain the most felsic glasses, although whole-rock compositions plot as andesites (except for **2K**). We estimate this is partly due to notably higher crystallinity (plagioclase + two-pyroxene + Fe-Ti oxides ± amphibole) of pumice compared to scoria but may also be due to imperfect separation of magma types due to mm- to μm-scale heterogeneities. Data for **2K** come from Tepley III *et al.* (2013) and additional whole-rock samples from all of Misti volcano's eruptive periods (gray circles) are compiled from Legros (2001), Ruprecht & Wörner (2007), and Rivera *et al.* (2017). A, andesite-trachyandesite; D, dacite-trachydacite; R, rhyolite.

pressures herein. Alkali feldspar and quartz stabilize at cooler temperatures than are observed in products of the Pacheco stage. Modeled melt compositions peak at ~72 wt.% SiO_2, below the most silicic glass compositions represented in $\mathbf{LR_R}$, $\mathbf{SI_R}$, $\mathbf{2K_R}$, and $\mathbf{M_{R2}}$ (up to 78 wt.% SiO_2). Models from this study are restricted to major elements but are consistent with limited FC. However, even though modeled FC trends span the compositional range of magmas with unimodal glass, units such as *A* exhibit trends at an angle to that of FC (Fig. 6) signaling differentiation by another process. Rivera *et al.* (2017) demonstrated that FC alone does not capture Misti's Sr and Nd isotopic trends, and assimilation of the local metamorphic basement (Charcani gneiss) is required, which has been similarly evidenced by distinct Pb isotopes (Barreiro & Clark, 1984; Davidson *et al.*, 1991). Ruprecht & Wörner (2007) also argue against FC as the main mechanism to explain plagioclase An–Fe variations, as sufficient elevation of Fe observed in the melt would require too large a percentage of FC. To account for the compositional range in Pacheco stage deposits, additional processes must be invoked (e.g. open system evolution via mixing). These models further support the suggestion that bimodal deposits are the result of distinct magmas mingling with each other prior to eruption.

In summary, observed glass compositions indicate the following:

1) Bimodal glass compositions within a single eruption with a large compositional range support the inference that intermediate magma recharge into a felsic magma body and subsequent mingling is an important process at Misti (i.e. **SI**, **SS**, **LR**, and **2K**).
2) Subtly contrasting bimodal glass compositions with a smaller compositional range may necessitate different explanations (i.e. **PI**, **M**). We suggest these characteristics result from either rejuvenation of a magma body with broadly similar compositions (Kent *et al.*, 2023), or a zoned magma chamber that undergoes convection and/or mingling of magmas upon eruption (e.g. Hildreth, 1981; Matthews *et al.*, 1999).
3) Magmas with unimodal glass compositions may acquire variability via hybridization of previously mingled magmas and/or minor cooling and FC (i.e. *A*, *PG*, *S*, *AP*).
4) Modeling suggests FC of andesitic melts is insufficient to produce the most felsic melts observed (72–78 wt.% SiO_2; $\mathbf{LR_R}$, $\mathbf{SI_R}$, $\mathbf{M_{R2}}$, $\mathbf{2K_R}$), and petrogenesis of the felsic melts requires other processes (e.g. crustal assimilation and/or melt extraction).

Mineral textures, compositions, and associated temperatures and pressures

Plagioclase

Within an eruption and across the Pacheco stage, plagioclase displays a range of compositions and textures (Figs. 7–10). Phenocrysts are ≤4 mm and dominantly euhedral-subhedral. Units including **SI**, **SS**, and **LR** contain anhedral crystals. For each unit, Table 1 summarizes the ranges and averages of An content of phenocrysts (>100 μm in size), and microlites (≤100 μm in size). Plagioclase range from oligoclase to bytownite ($An_{25–88}$), but most are andesine to labradorite ($An_{40–70}$) (Fig. 9a) (Tepley III *et al.*, 2013). The widest An range occurs in deposits with strong bimodal glass distributions (**SI**, **SS**, **LR**, and **2K**), and the range in An for a deposit correlates generally to the SiO_2 (wt.%) of that deposit's glass. Figure 7c shows stacked histograms for analyses from plagioclase cores, mantles, and rims from each unit. Cores tend to exhibit the

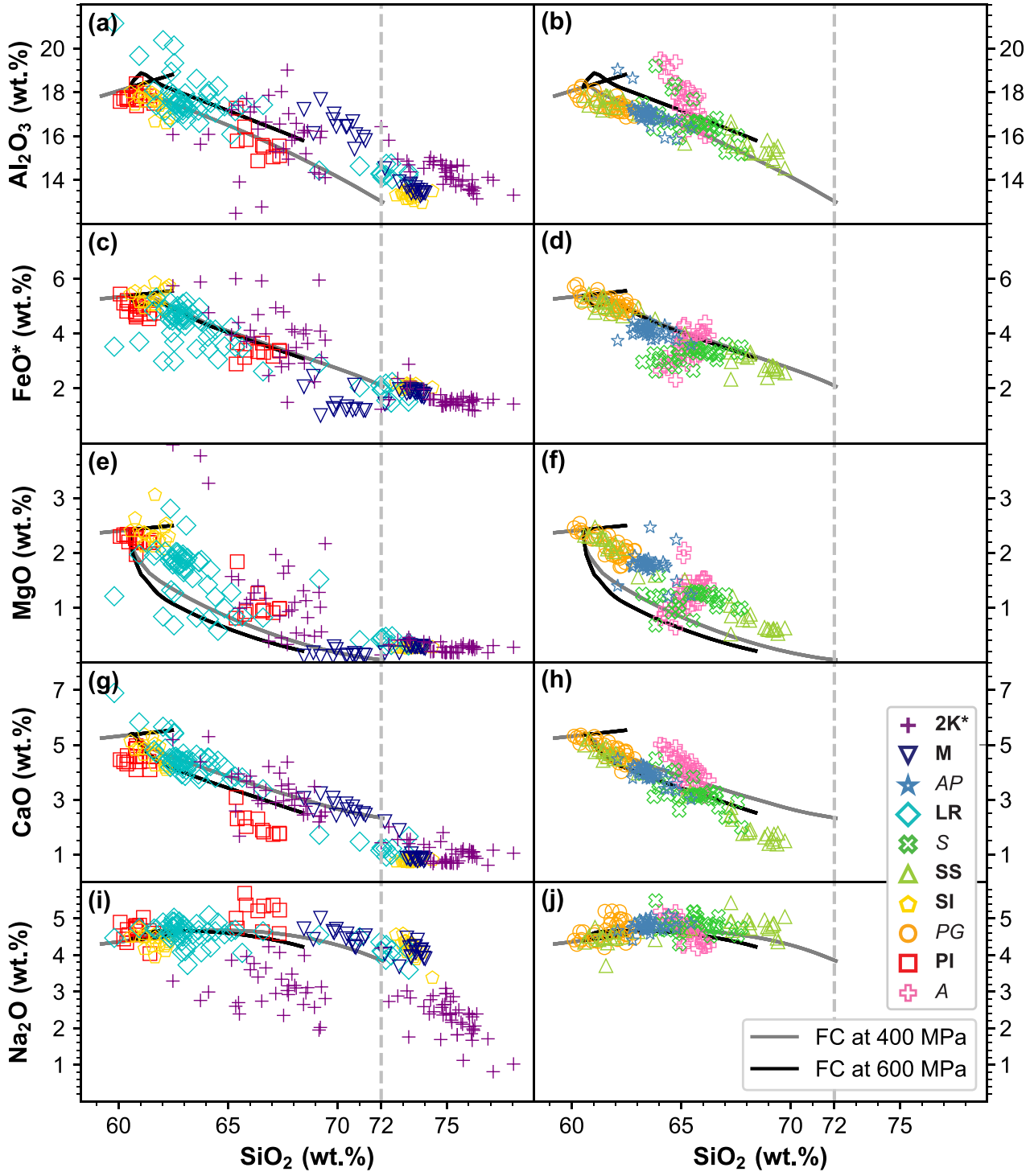

Fig. 6. Select major oxide diagrams illustrating glass compositions for bimodal (left column) and unimodal (right column) glass deposits. Plotted against SiO_2 by wt.% are: Al_2O_3 (a-b), FeO* (c-d), MgO (e-f), CaO (g-h), and Na_2O (i-j). Gray and black solid lines show fractional crystallization (FC) models performed at 400 and 600 MPa, respectively, and dashed line shows maximum SiO_2 reached in models (72 wt.%). Models proceed from low to high SiO_2 and all compositions are anhydrous normalized to 100%. Note the slope of Autopista (pink plus signs) data trends are at a moderate-high angle to FC trends.

highest An and some deposits show single peak positions of An (e.g. *AP*), whereas others have multiple peaks (e.g. **LR**). Three broad plagioclase populations are distinguished based on An content. All are persistent throughout the Pacheco stage, including: type I, high-An plagioclase; type II, moderate-An plagioclase; and type III, low-An plagioclase, which are further divided into subcategories using crystal textures (Table 2 and Fig. 8a-i). A single crystal can consist of multiple plagioclase types. Rather than classify entire crystals, we emphasize the constituent parts (e.g. distinct growth zones) observed in different units.

Type I plagioclase High-An plagioclase range from $An_{74–88}$ and are present but generally sparse in all units. Notably, type I plagioclase reside almost exclusively in crystal cores. BSE images reveal they are sometimes clear (type Ia), but often show patchy

Table 1: Summary of phases by unit and their associated characteristics. Unit names in italic denote an eruption with unimodal glass chemistry, while those in bold indicate an eruption with largely bimodal glass chemistry

Unit	Phases (volume%)	Phase Characteristics
Autopista (A_D)	glass (32–48%)	A_D: 61–66 wt % SiO_2
	plagioclase (8–12%)	phenocrysts: $An_{33–83}$, avg. An_{62}; microlites: $An_{35–69}$, avg. An_{53}
	amphibole (3–5%)	pargasite to edenite; reacted and unreacted crystals present within same sample; rim thickness varies substantially; crystals are commonly zoned
	pyroxene (<1%)	augite and enstatite; no touching pairs; cpx Mg# 67–80, avg. 74
	Fe-Ti oxides (1%)	Fe-Ti oxides present as touching pairs
	vesicles (40–50%)	typically fine, round, and evenly distributed
Ponche Iridescente (**PI_A, PI_D**)	glass (31–54%)	**PI_A**: 60–62 wt % SiO_2 **PI_D**: 65–67 wt % SiO_2
	plagioclase (3–15%)	phenocrysts: $An_{34–84}$, avg. An_{62}; microlites: $An_{45–67}$, avg. An_{60}
	amphibole (<1%)	unreacted pargasite; zoned and unzoned
	pyroxene (2–3%)	augite and enstatite; present singularly or as touching pairs; cpx Mg# 73–80, avg. 77
	Fe-Ti oxides (1%)	Fe-oxides dominate; Ti-oxides rare; rare touching pairs
	olivine (trace)	$Fo_{79–80}$
	vesicles (40–50%)	round to subround; average 0.5 mm or less but up to a few mm
Ponche Gris (PG_A)	glass (38–56%)	PG_A: 60–63 wt % SiO_2
	plagioclase (10–15%)	phenocrysts: $An_{50–83}$, avg. An_{64}; microlites: $An_{62–75}$, avg. An_{66}
	amphibole (1%)	unreacted pargasite; zoning rare
	pyroxene (2–5%)	augite and enstatite; present singularly or as touching pairs; cpx Mg# 67–80, avg. 76
	Fe-Ti oxides (1%)	Fe-oxides dominate; Ti-oxides rare; rare touching pairs
	vesicles (30–40%)	contains small subround (<0.1 mm) and large irregular (0.3–2.0 mm) populations
Sandwich Inferior (**SI_A, SI_R**)	glass (39–61%)	**SI_A**: 61–62 wt % SiO_2 **SI_R**: 73–74 wt % SiO_2
	plagioclase (7–15%)	phenocrysts: $An_{25–83}$, avg. An_{61}; microlites: $An_{25–80}$, avg. An_{55}
	amphibole (<1%)	unreacted pargasite; largely rounded and zoned crystals
	pyroxene (1–4%)	augite and enstatite; present singularly or as touching pairs; cpx Mg# 71–81, avg. 75
	Fe-Ti oxides (1–2%)	Ti-oxides common in **SI_R** and sparser in **SI_A**; present as touching pairs
	vesicles (30–40%)	contains small subround (<0.05 mm) and large irregular (>0.3 mm) populations
Sandwich Superior (**SS_{AD}, SS_{DR}**)	glass* (25–36%)	61–70 wt % SiO_2 **SS_{AD}**: ~61–62 wt % SiO_2 **SS_{DR}**: ~68–70 wt % SiO_2
	plagioclase (10–20%)	phenocrysts: $An_{30–81}$, avg. An_{59}; microlites: $An_{31–67}$, avg. An_{52}
	amphibole (<1%)	pargasite to edenite; reacted and unreacted crystals present within same sample; many crystals zoned
	pyroxene (2–3%)	augite and enstatite; present singularly or as touching pairs; cpx Mg# 69–81, avg. 77
	Fe-Ti oxides (1%)	Ti-oxides common in **SS_{DR}** and sparser in **SS_{AD}**; present as touching pairs
	vesicles (50%)	More evenly distributed and equal in size in **SS_{DR}** than **SS_{AD}**, which has bimodal distribution of sub-mm and mm-sized vesicles
Sancayo (S_D)	glass (44–53%)	S_D: 64–68 wt % SiO_2
	plagioclase (3–10%)	phenocrysts: $An_{40–79}$, avg. An_{54}; microlites: $An_{46–56}$, avg. An_{52}
	amphibole (1–2%)	unreacted pargasite to edenite; most crystals zoned
	pyroxene (2–3%)	augite and enstatite; present singularly or as touching pairs; cpx Mg# 68–83, avg. 75
	Fe-Ti oxides (1%)	present as touching pairs
	olivine (trace)	Fo_{77}
	vesicles (40%)	some samples show uneven vesicle distribution; otherwise, sub-mm sized
La Rosada (**LR_{AD}, LR_R**)	glass (13–43%)	**LR_{AD}**: 61–67 wt % SiO_2 **LR_R**: 71–73 wt % SiO_2
	plagioclase (5–20%)	phenocrysts: $An_{32–82}$, avg. An_{65}
	amphibole (5–8%)	pargasite; reacted and unreacted crystals present within same sample; zoning common
	pyroxene (1–3%)	augite and enstatite; present singularly or as touching pairs; cpx Mg# 68–81, avg. 75
	Fe-Ti oxides (1%)	Ti-oxides common in **LR_R** and sparse in **LR_{AD}**; present as touching pairs
	vesicles (45–55%)	very fine (<0.1 mm) in **LR_R** and bimodal distribution of sub-mm and mm-sized vesicles in **LR_{AD}**
Apo (AP_{AD})	glass (41–48%)	AP_{AD}: 62–65 wt % SiO_2
	plagioclase (7–12%)	phenocrysts: $An_{48–75}$, avg. An_{59}; microlites: $An_{51–59}$, avg. An_{55}
	amphibole (1%)	unreacted pargasite; zoning ubiquitous
	pyroxene (3–5%)	augite and enstatite; present singularly or as touching pairs; cpx Mg# 73–84, avg. 76
	Fe-Ti oxides (1%)	present as touching pairs
	vesicles (40%)	bimodal distribution of sub-mm and mm-sized vesicles

(Table continues)

and/or coarsely sieved textures with either abrupt and straight or resorbed boundaries (type Ib). We interpret these to be antecrysts sourced from earlier pulses of mafic magma from deeper in Misti's storage system.

Type II plagioclase Moderate-An plagioclase ($An_{50–73}$) is the most prevalent population overall. When a crystal is composed of a single plagioclase type, it is most often that of type II. Oscillatory (low amplitude, high frequency) zoning is often present (type IIa), but

Table 1: Continued

Unit	Phases (volume%)	Phase Characteristics
Misquirichi ($\mathbf{M_{R1}}$, $\mathbf{M_{R2}}$)	glass (47–51%)	$\mathbf{M_{R1}}$: 68–71 wt % SiO_2 $\mathbf{M_{R2}}$: 73–74 wt % SiO_2
	plagioclase (5–7%)	phenocrysts: $An_{41–74}$, avg. An_{65}; microlites: $An_{26–63}$, avg. An_{51}
	amphibole (2–3%)	pargasite to edenite; reacted and unreacted crystals present within same sample; zoning common
	pyroxene (1–2%)	augite and enstatite; present singularly or as touching pairs; cpx Mg# 69–80, avg. 76
	Fe-Ti oxides (1%)	present as touching pairs
	vesicles (40%)	bimodal distribution of sub-mm and mm-sized vesicles
2000 BP ($\mathbf{2K_D}$, $\mathbf{2\ K_R}$) (data from Tepley *et al.*, 2013)	glass (40%)	$\mathbf{2K_D}$: 62–69 wt % $\mathbf{2K_R}$: 72–78 wt %
	plagioclase (6%)	phenocrysts: $An_{30–88}$; microlites: $An_{28–63}$
	amphibole (2%)	pargasite to edenite; reacted and unreacted crystals present within same sample
	pyroxene (1%)	augite and enstatite; no touching pairs; Mg# ~75
	Fe-Ti oxides (1%)	present as touching pairs
	vesicles (50%)	heterogenous vesicle sizes and distributions in $\mathbf{2K_R}$; typically equant to sub-spherical vesicles in $\mathbf{2K_D}$

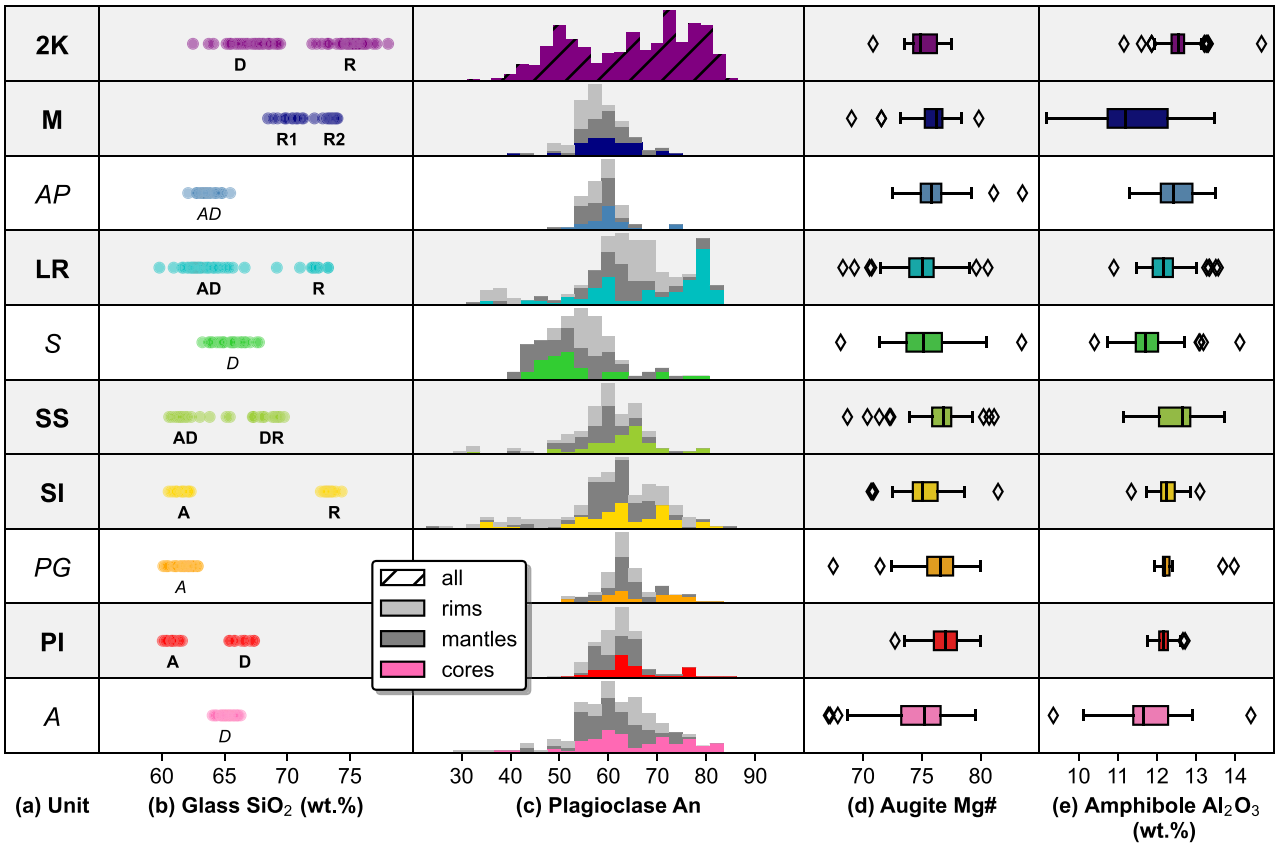

Fig. 7. Summary of key Pacheco stage geochemistry in stratigraphic order. Rows with white and gray backgrounds are to highlight hybridized and mingled units, respectively. (a) Stratigraphy with unit abbreviations as in Fig. 3 from oldest (*A*) to youngest (**2K**). (b) Glass SiO_2 (wt.%) contents measured via electron microprobe from all tephra types distinguishable in hand sample. Note the alternation between eruption of hybridized (unimodal) and mingled (bimodal) glasses. A, andesite-trachyandesite; D, dacite-trachydacite; R, rhyolite. (c) Stacked histograms of plagioclase anorthite content (An) from core (colored), mantle (dark gray), and rim (light gray) analyses. Units with the most distinctly bimodal glasses correspond to the widest range of An (e.g. **SI**, **SS**, **LR**, and **2K**) and units that lack a felsic glass also lack low-An (<An_{50}) crystals (e.g. **PI**, *PG*, *AP*). (d) Boxplots of augite Mg# (=$(Mg/Fe+Mg)_{atomic}$*100), which remains relatively constant throughout the stratigraphic section. (e) Boxplots of amphibole Al_2O_3 (wt.%). Amphibole compositions remain relatively similar, with Al_2O_3 typically >10 wt.%. Diamonds in boxplots represent outliers.

there are many cases of high-amplitude, low-frequency zoning as well (type IIb). It is not uncommon for plagioclase to contain resorption surfaces crosscutting multiple zones. Entire crystals or crystal zones may also be coarsely sieved (IIc) or relatively clear (IId). We interpret type II plagioclase to be phenocrysts sourced from the dominant intermediate magmas recorded in the Pacheco stage.

Type III plagioclase Low-An ($An_{25–49}$) populations are rare to absent in units that lack a relatively silicic liquid (**PI** and *PG*) and are prevalent in units with the most silicic liquids (e.g. **SI** and **LR**).

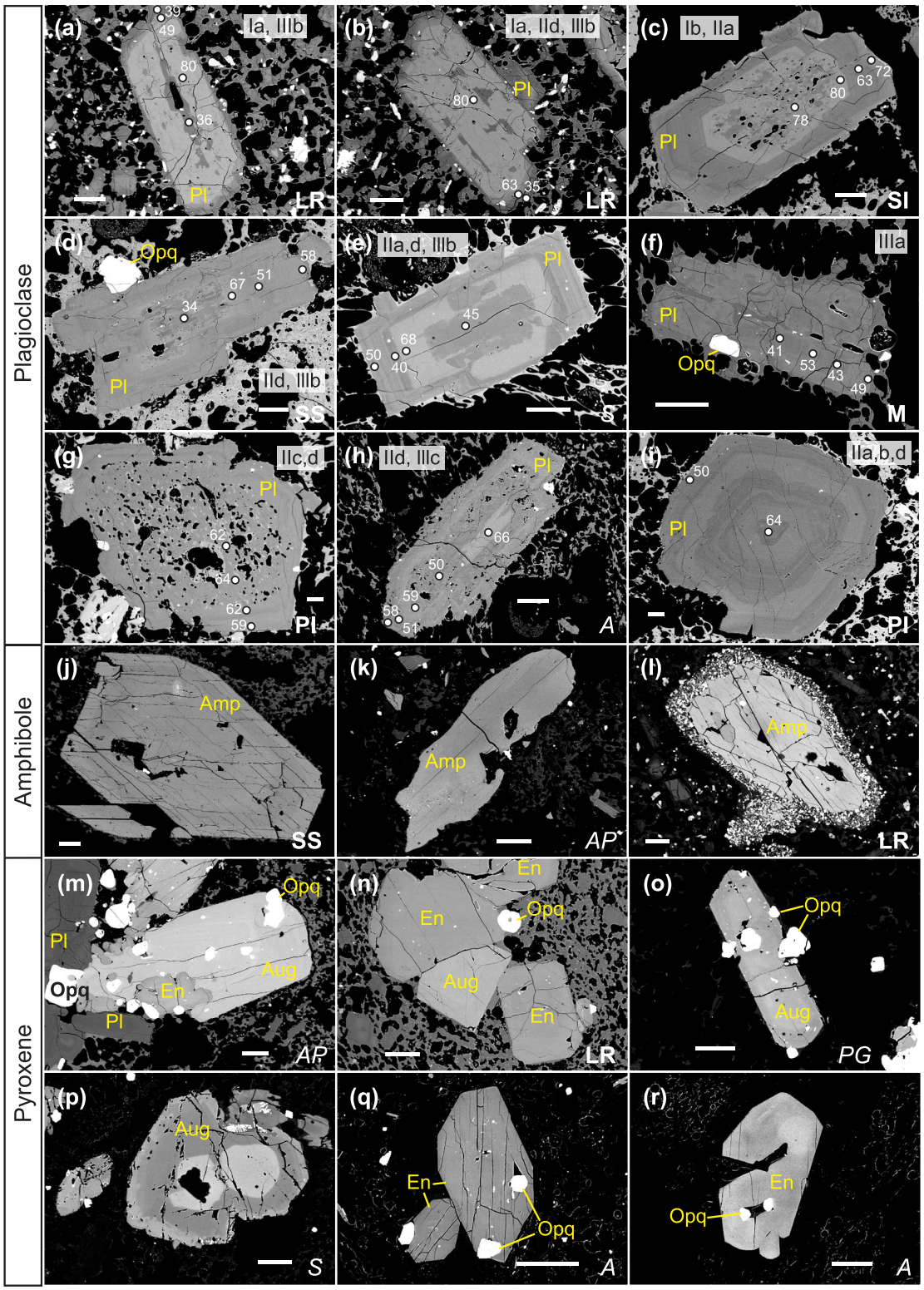

Fig. 8. Backscattered electron images of representative Pacheco stage plagioclase, amphibole, and pyroxene. Plagioclase type corresponding to Table 2 and anorthite content (An; numbered circles) are indicated. Scale bars represent 100 μm. (a) coarsely sieved plagioclase (Pl) with high-An interior, (b) plagioclase encapsulating all three crystal types (high-, moderate-, and low-An), (c) plagioclase with sieved and patchy high-An core followed by growth of moderate-An mantle and rim, (d) plagioclase with patchy and resorbed low-An core followed by growth of moderate-An, (e) plagioclase illustrating repeat crystal exchange between felsic and intermediate magmas, (f) patchy low-An plagioclase, (g) coarsely sieved moderate-An plagioclase, (h) plagioclase with resorbed core and sieved mantle, (i) oscillatory-zoned plagioclase recording several resorption events, (j) largely euhedral amphibole (Amp) with subtle diffuse zoning, (k) anhedral amphibole crystal with patchy diffuse zoning and embayments, (l) reaction rim (plagioclase + pyroxene + Fe-Ti oxides) on amphibole, (m) glomerocryst of plagioclase + augite (Aug) + enstatite (En) + opaques (Opq), (n) enstatite + augite + opaques glomerocryst, (o) diffusely zoned augite with opaque inclusions, (p) augite cluster containing both normal and reverse zoning defined by sharp and diffuse boundaries, respectively, (q) largely unzoned euhedral enstatite with opaque inclusions, and (r) subhedral and embayed enstatite with patchy zoning.

Table 2: Summary of plagioclase types found in tephra-fall deposits from the Pacheco stage

Type	Characteristics	Occurrence and Interpretation
I - High-An ($An_{74–88}$) plagioclase		
	Clear (Ia) or coarsely sieved crystals (Ib) Patchy textures sometimes present	Present in all units but sparse Exclusive to crystal cores Most common in **LR** of all units Antecrystic cores sourced from relatively mafic magma
II - Moderate-An ($An_{50–73}$) plagioclase		
	Oscillatory (low amplitude, high frequency) zoned crystals (IIa), high amplitude, low frequency zoned crystals (IIb), coarsely sieved crystals (IIc), and/or relatively clear crystals (IId) Zones may be defined by resorption surfaces that crosscut multiple boundaries	Present in all units and dominant plagioclase type Complex textures evident of dynamic magma conditions Phenocrysts sourced from dominant intermediate magma
III - Low-An ($An_{25–49}$) plagioclase		
	Clear crystals or zones (IIIa), discontinuous blocky zones (IIIb), or rounded, irregular, and dusty resorbed (IIIc) zones Type IIIb fill in sieved voids in Types I or II plagioclase Type IIIc are enveloped by Types I or II plagioclase	Associated with units with a relatively felsic glass Absent in **PI** and *PG* Phenocrysts sourced from minor felsic magma

When present, this population is typically clear and lacks sieved textures (IIIa). A subset exists as blocky disjointed patches in type I or II plagioclase (IIIb), or have rounded and irregular dusty low-An plagioclase zones (IIIc) surrounded by growth of type II plagioclase. We interpret type III plagioclase to represent phenocrysts grown in a transient felsic magma.

Plagioclase trace element systematics Disequilibrium textures and zoning present in crystals from Pachecho stage deposits highlight the sensitivity of plagioclase to dynamic magma chamber and crystallization conditions (Singer *et al.*, 1995; Tepley III *et al.*, 1999; Ginibre *et al.*, 2002a, 2002b, 2007; Landi *et al.*, 2004; Ruprecht & Wörner, 2007). Plagioclase compositions are controlled largely by temperature, melt composition, and H_2O content (Bowen, 1928; Tsuchiyama, 1985; Housh & Luhr, 1991). Whereas all three variables change An, and thus An alone is inadequate to distinguish between compositional controls, trace element concentrations such as Mg and Fe are largely controlled by melt composition (Ginibre *et al.*, 2007; Ginibre & Wörner, 2007). Convective currents and self-mixing (Singer *et al.*, 1995; Couch *et al.*, 2001) or thermal mixing (Ruprecht & Wörner, 2007) in a closed system may produce crystals with An zoning, but without input of a disparate magma, trace element trends remain relatively constant. In contrast, open-system recharge events also change melt compositions, resulting in new equilibrium partitioning conditions and crystals zoned in major and trace elements. As such, it is possible to use trace element compositions to discern between crystal populations.

Ruprecht & Wörner (2007) interrogated plagioclase in volcanic deposits spanning Misti's entire history with a focus on Fe-An variations across resorption boundaries, and identified trends produced by both thermal and compositional mixing. They report mostly flat Fe-An correlations (steady Fe with changing An) and conclude thermal and cryptic mixing dominate Misti's system. Similarly, Mg and Fe trace element transects were measured in plagioclase in *A*, **PI**, and **LR** via LA-ICP-MS coupled with major elements via EMP (Electronic Appendix 4). Figure 10 plots this dataset shaded by An density, which broadly highlights separate An groups in mingled units (**PI** and **LR**) and a single dominant population in the hybridized unit (*A*). We also model equilibrium-partitioning plagioclase trace element concentration curves using Mutch *et al.* (2022) for Mg (M22) and Bindeman *et al.* (1998) for Fe (B98). The least and most silicic glass compositions in our dataset are used to calculate the intermediate (60 wt.% SiO_2, 2.5 wt.% MgO, 6.0 wt.% FeO at 1000°C) and felsic (77 wt.% SiO_2, 0.2 wt.% MgO, 2.0 wt.% FeO at 800°C) curves. Identical curves are shown for all units in Fig. 10, and Fig. 10c-d insets highlight subtle variations in **PI** plagioclase. An-Fe exhibits global positive correlations, whereas An-Mg shows slightly positive correlations for **LR** and **PI** and relatively constant Mg at varying An in *A*. Two-thirds of individual transects record positive An-Fe and An-Mg correlations linked to major An increases. Although many correlations have slopes similar to the 'slightly positive' case of Ruprecht & Wörner (2007) (see their Table 3 and Fig. 7a), which can be explained by changes in fO_2 estimated for Misti, there is a subset with steeper An-Fe trends that must involve another process such as changing melt compositions (Fig. 11). The interpretation of An-Mg trends is complicated by the inflection in partitioning curves (Mutch *et al.*, 2022). However, when coupled with An-Fe trends and additional chemical and textural evidence, we prefer a model of recharge, mingling, and hybridization as explanation.

We use **LR**, **PI**, and *A* plagioclase to exemplify endmember scenarios observed in the Pacheco stage. We examine **LR** as the simplest and most distinct example of crystal exchange between three distinct magmas via recharge and mingling. **PI** has a narrower range of plagioclase An but still displays robust evidence of magma mingling and crystal exchange under different circumstances (i.e. rejuvenation or perhaps a weakly zoned magma lens). Finally, we scrutinize *A* as an example of a hybridized magma.

An example of magma recharge and mingling: La Rosada **LR** plagioclase display population clusters centered at approximately An_{40} (type III), An_{60} (type II), and An_{80} (type I) (Fig. 7c and 10a-b). Type I plagioclase exhibits high Fe (3500–6000 ppm) and moderate Mg (200–450 ppm), type II plagioclase exhibits moderate Fe (3000–5000 ppm) and high Mg (200–500 ppm), and type III plagioclase contains low Fe and Mg (2500–3500 and 100–300 ppm, respectively). As presented above, we infer the low-, moderate-, and high-An populations correlate to broadly felsic, intermediate, and mafic magmas, respectively. This is further supported by the observation that type III plagioclase fall along or below the M22 and B98 felsic melt equilibrium lines, type I plagioclase fall near or above the M22 and B98 intermediate melt equilibrium lines, and type II plagioclase span between them (Fig. 10a-b). Crystals

containing highly contrasting An (>20 mol%) across boundaries are present and unlikely to result from local effects (e.g. Ginibre *et al.*, 2002b), and single crystals can span nearly the entire observed An range (Fig. 8b shows **LR** plagioclase with zones of An_{80}, An_{63}, and An_{35}).

We envision that these crystals record a multistage history of magma recharge, mingling, and hybridization. High-An plagioclase are restricted to crystal cores and their trace element systematics discussed above (e.g. Fig. 9b) are consistent with the interpretation that they crystallize from the deepest relatively mafic magma associated with this eruption. At some point, recharge initiates mixing with overlying intermediate magma. The abrupt temperature drop as this magma comes into contact with cooler magma creates supercooled conditions and coarsely sieved plagioclase form via skeletal growth (Kawamoto, 1992), and high-An crystals are interspersed into an intermediate melt where moderate-An rims form (Fig. 8c). Since mafic melt is not sampled by any eruption in the Pacheco stage, we surmise these mafic and intermediate melts hybridize. The moderate-An population exists as discrete subhedral-anhedral, coarsely sieved crystals or as zones or rims in other crystals. Limited oscillatory zoning and zoning with minor resorption surfaces indicate this magma may undergo convection (Ginibre *et al.*, 2002b), self-mixing (Couch *et al.*, 2001), or thermal mixing (Ruprecht & Wörner, 2007) due to contemporaneous thermal underplating of the intermediate magma by the mafic magma. This would favor progressive hybridization of the melts from these magmas as temperatures equilibrate and viscosity differences lessen (e.g. Ruprecht *et al.*, 2012). This hybridized magma batch carries crystal cargo dominated by intermediate-An plagioclase and high-An antecrysts. The slope of global An-Mg trace element systematics between types I and II plagioclase follows the negative slope of the predicted intermediate magma equilibrium lines (Fig. 10a), suggesting type I plagioclase had time to equilibrate under type II plagioclase conditions. Diffusion of Mg is about three times faster than Fe in plagioclase (Costa *et al.*, 2003), and An-Fe systematics suggest type I plagioclase Fe equilibration has not occurred. These zones record only the first of two mixing events.

The hybridized magma and its crystals must ascend more through the crust, mixing a second time upon reaching overlying cooler felsic magma. Upon injection, the recharge magma is forced again to cool, and extensive sieve textures form throughout moderate-An plagioclase. Conversely, the felsic magma body's low An-Mg-Fe plagioclase are heated by the recharge magma above their liquidus temperatures and are initially largely resorbed (Tsuchiyama, 1985), as evidenced by rare type III plagioclase. This phenomenon is documented in mixing experiments by Laumonier *et al.* (2014), which demonstrate most felsic-derived plagioclase should melt upon mixing with mafic magma. However, preservation of some low-An phenocrysts shows recharge-induced thermal excursions are transient (Laumonier *et al.*, 2014). We interpret blocky patches of low-An interiors seemingly enveloped by high-An crystals (e.g. Fig. 8a) to reflect infilling of skeletal high-An plagioclase by low-An plagioclase upon dispersal into felsic magma. Since glass chemistry indicates that the mafic melt that crystallized high-An plagioclase does not survive to eruption, it is unlikely that crystallization of high-An plagioclase around low-An cores occurs at shallow depths. After crystal resorption and exchange, low-An rims grow on high- and moderate-An plagioclase. Moderate-An plagioclase dominates and the intermediate magma is likely the most volumetrically significant magma, while low-An plagioclase is rare and often found on the rims of crystals, which signals interaction with

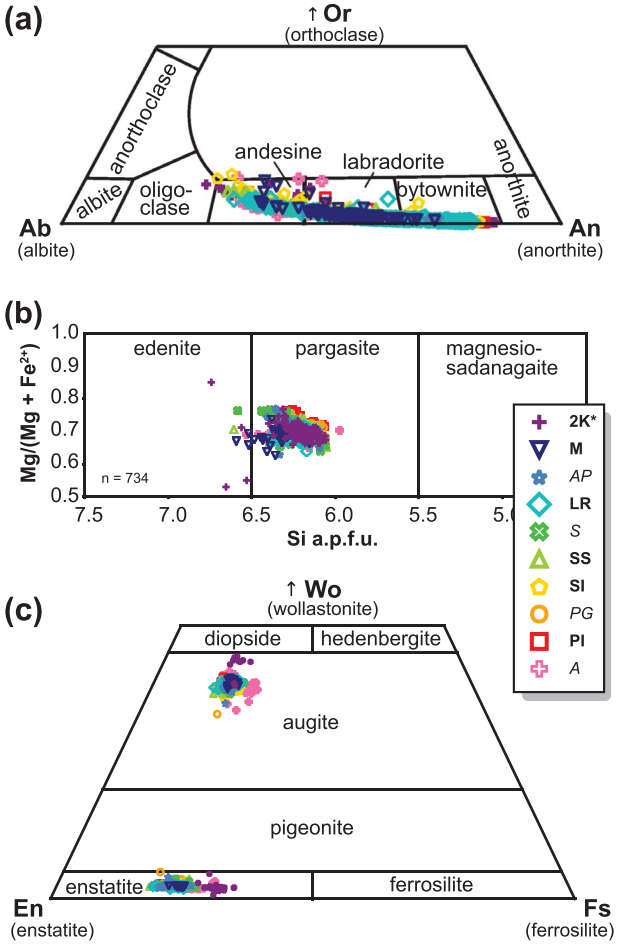

Fig. 9. Classification diagrams for (a) plagioclase (after Deer *et al.*, 1992), (b) amphibole (after Leake *et al.*, 1997), and (c) pyroxene (after Deer *et al.*, 1992). Plagioclase range from oligoclase to bytownite but are most commonly labradorite. Amphibole are pargasite with ten edenite compositions recorded. Augite and enstatite generally plot in tight clusters except for variability within *A* and **2K** pyroxene.

felsic magma is a late-stage process. As opposed to type I plagioclase trace element systematics, which suggest time has passed for Mg (but not Fe) equilibration with an intermediate magma to occur, types II and III plagioclase do not fall along similar equilibration trends (Fig. 10a-b). Plagioclase growth in areas of hybridized melt is reflected by plagioclase compositions spanning between the intermediate and felsic equilibrium lines, as well as samples containing a range of An-Fe slopes as in Ruprecht & Wörner (2007). Finally, reflected by preservation of disparate melt compositions, mixing was interrupted by eruption. Based on similar textural and compositional trends, we envision comparable histories for **SI** and **SS**, as has been similarly demonstrated for **2K** (Tepley III *et al.*, 2013).

An example of magma rejuvenation and mingling: Ponche Iridescente

PI represents a subtler mingling endmember from rejuvenation of one intermediate magma by another or possibly a weakly zoned magma chamber disturbed prior to eruption. Contrasts between mingled glasses are much lower compared to **LR,** ranging from 60–62 ($\mathbf{PI_A}$) and 65–68 ($\mathbf{PI_D}$) wt.% SiO_2. Except for type I plagioclase cores, plagioclase compositional differences are also less pronounced; they are generally of type II and fall near the intermediate magma equilibrium curves (Fig. 10c-d). However, **PI**'s An-Mg and An-Fe systematics indicate two moderate-An

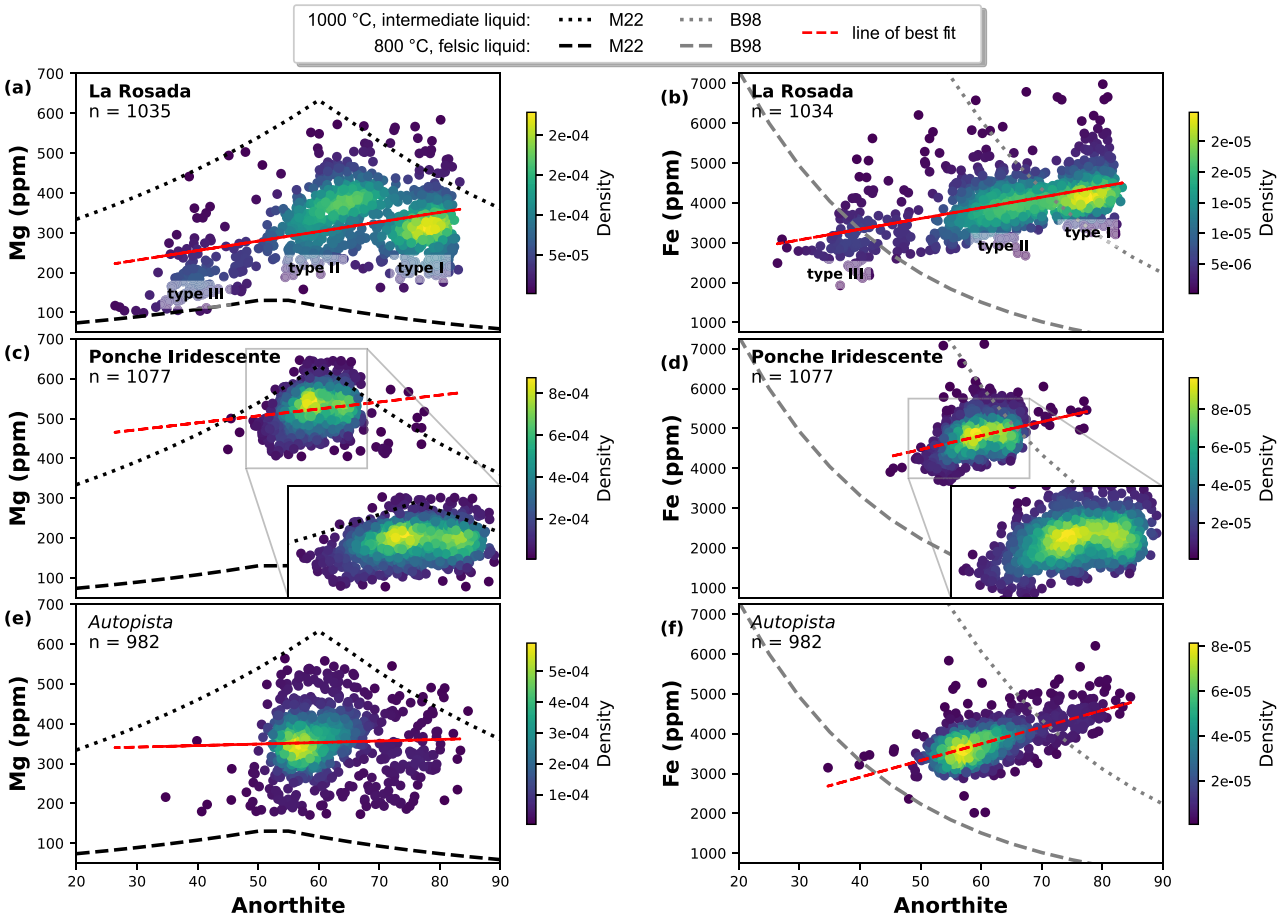

Fig. 10. Anorthite (An) versus trace element contents (Mg and Fe in ppm) in plagioclase transects from (a-b) **LR**, (c-d) **PI**, and (e-f) *A*. Symbols represent individual plagioclase analyses. Data are colored by point density across the plot area, which broadly highlights the existence of separate An groups in mingled units (**PI** and **LR**) and a single dominant population in the hybridized unit (*A*). Insets in (c-d) highlight subtle compositional differences in **PI** plagioclase. Also shown are equilibrium concentration curves calculated using Mutch *et al.* (2022) for (M22) and Bindeman *et al.* (1998) for Fe (B98). The least and most silicic glasses in our dataset are used to determine intermediate (60 wt.% SiO_2, 2.5 wt.% MgO, 6.0 wt.% FeO at 1000°C) and felsic (77 wt.% SiO_2, 0.2 wt.% MgO, 2.0 wt.% FeO at 800°C) melt equilibrium partitioning curves. Note that the trendline of Fe versus An in all deposits is positively correlated, suggesting changes in bulk magma composition over the crystallization of these units' plagioclase. Global An-Mg trends suggest some diffusive equilibration has taken place in **PI** and between type I and II plagioclase in **LR** (following the intermediate melt equilibrium line), although this is not true for all individual transects.

populations at ranges of ~$An_{50–60}$ with 400–650 ppm Mg and 3500–6000 ppm Fe versus ~$An_{60–70}$ with 450–650 ppm Mg and 4000–6000 ppm Fe. Trace element ranges for each population are similar, but there is a weak positive correlation with An versus Fe and Mg. We infer the $An_{50–60}$ crystals grew in the slightly more felsic $\mathbf{PI_D}$ and the $An_{60–70}$ crystals grew in a slightly less evolved $\mathbf{PI_A}$. Matching textures and compositions to plagioclase in Fig. 8i are traced across a large subset of **PI**'s crystals, implying they experienced similar conditions that were not simply from local effects. A few of these crystals' cores are patchy or irregular high-An plagioclase. Otherwise, crystal interiors record both high and low frequency oscillatory zoning with several minor resorption events. Midway through the interior is the most An-poor zone followed by a major irregular resorption surface cutting through several growth zones. Growth after this disruption is up to 11% more An-rich. Most crystal rims fall into a narrow range of $An_{58–62}$.

PI plagioclase again record a multistage history of mingling. Similar to **LR**, some crystal cores are high-An antecrysts from a mafic magma that were interspersed into an overlying intermediate magma, this time represented by the ~$An_{60–70}$ group upon which zones of this composition grew. Subsequent ascension of magma carrying $An_{60–70}$ plagioclase recharged and mingled with magma hosting $An_{50–60}$ plagioclase. This perturbation to the system is signaled by a major resorption surface, after which plagioclase up to 11% more An-rich grew. Evidence for some amount of hybridization of the two melts before eruption exists as rim compositions that fall within a narrow compositional range ($An_{58–62}$), approximating the average of both populations. This growth is disrupted upon eruption. Alternatively, these plagioclase represent a once-stable zoned magma chamber disrupted by a recharge event. Although an eruption is initiated, the recharge magma at the chamber base is not sampled in the eruption. The recharge may only act to underplate and heat the overlying magmas (Ruprecht & Wörner, 2007) and add mass and volatiles to the chamber. The magmas mingle more through the conduit to produce observed glass and plagioclase characteristics. Plagioclase compositions and textures of **M** suggest a similar history, although the magmas involved are more silicic.

An example of magma recharge and hybridization: Autopista Lastly, A's groundmass glass (A_D) represents a homogenous intermediate melt that contains intermediate plagioclase compositions centered around ~An_{60} (Figs. 7b-c). The main peak at ~An_{60}

suggests many of A's plagioclase crystallized from an intermediate magma. Even so, A_D contains type I high-An plagioclase cores suggesting a history of mixing similar to those discussed above. The broad range of plagioclase compositions from $An_{30–83}$ also mimics the ranges in bimodal magmas such as **LR** and **SI**, with low-An plagioclase possibly crystallizing from a felsic melt. Furthermore, over two-thirds of rimward transects that record major An changes also record a positive correlation for An versus Fe and Mg (Electronic Appendix 4), which indicate one of the final incidents documented by plagioclase in a seemingly homogenous magma was recharge. Based on these observations, the single range of glass compositions suggests the mixing dynamics were such that hybridization of the erupted magma was generally favored, but magma recharge was still one of the final events recorded a subset of the plagioclase. Eruption of magma such as that which supplied *A* may be triggered similarly to **PI** since a recharge magma was not sampled by the eruption. The hybridized characteristics of *PG*, *S*, and *AP*'s melts and relatively narrow ranges of An and trace elements suggest similar histories for magmas supplying these eruptions.

Plagioclase thermometry We apply the thermometer of Putirka (2008, equation 24a) to plagioclase-liquid pairs from each deposit, pairing all plagioclase analyses with the two modes of glass compositions separately in bimodal units. We utilize the matrix matching function of Thermobar (Wieser *et al.*, 2022) to test all plagioclase-liquid pairs and use only those in chemical equilibrium to estimate temperatures. Estimates using the least evolved and hybridized glass compositions record temperatures of ~950–1000°C (Fig. 12c), and temperature estimates are consistently cooler (~800–925°C) when using the more silicic glass compositions (Fig. 12d).

Chemical and textural characteristics of plagioclase are key for interpreting the petrology of Misti's magmas. The major conclusions drawn from Pacheco stage plagioclase here are:

1) High- (type I), moderate- (type II), and low-An (type III) crystals and/or growth zones and their trace element systematics broadly correlate to mafic, intermediate, and felsic magma types, respectively. The large range in temperatures recorded by plagioclase-liquid thermometry is consistent with this idea.
2) Moderate-An compositions are most common and indicate the dominant magma sampled by these eruptions is intermediate.
3) The combination of plagioclases textures and trace element systematics supported by melt compositions delineates a multistage history of magma recharge and mixing.
4) High- and moderate-An cores and interior zones associated with coarsely sieved textures (types Ib and IIc) indicate these crystals underwent resorption (Kuno, 1950; Dungan & Rhodes, 1978; Gerlach & Grove, 1982; Nelson & Montana, 1992) or rapid growth (Kuo & Kirkpatrick, 1982; Anderson, 1984; Kawamoto, 1992) prior to growth of their next zone or rim. Because we infer these crystals are staged at different levels in the crust and brought together with crystals of different populations initially upon mixing events, we surmise that these textures can either be the result of the ascent of their host magmas to lower pressures and/or undercooling.
5) Dusty plagioclase (type IIIc) form via dissolution when less calcic plagioclase contacts melt in equilibrium with more calcic plagioclase (Tsuchiyama, 1985), consistent with evidence of compositionally distinct magmas mixing.
6) Reversely zoned crystals with low-An cores or mantles are sparse in **LR**. Since this deposit records recharge from a more mafic magma, we infer that many low-An crystals were resorbed after mixing (Laumonier *et al.*, 2014). Blocky low-An patches in crystal cores (type IIIb) likely represent infilling of high-An skeletal or coarsely sieved antecrysts by low-An growth after initial heating effects.

Amphibole

Amphibole is present in all Pacheco stage units with abundances ranging from <1–8 volume% (Table 1). Four observed amphibole textures include (Fig. 8j-l): (1) euhedral-subhedral crystals; (2) crystals with reaction rims of plagioclase + pyroxene + Fe-Ti oxide microlites; (3) subhedral-anhedral rounded-embayed crystals; and (4) diffusely zoned crystals. Crystals with reaction rims are commonly but not always hosted in the more silicic melt of a bimodal unit. Sparse amphibole occur as glomerocrysts. They are frequently associated with oxides, sometimes with plagioclase, and are touching pyroxenes only in *A*. In the Sandwich deposits, amphibole is only hosted in $\mathbf{SI_A}$ and $\mathbf{SS_{AD}}$. Possible remnants of reacted amphibole in $\mathbf{SI_R}$ and $\mathbf{SS_{DR}}$ exist; however, the crystals in question are small and difficult to identify. Based on >700 spot analyses and nomenclature of Leake *et al.* (1997), amphibole are pargasites with just ten edenite compositions (Fig. 9b). Amphibole Al_2O_3 consistently ranges from ~11 to 14 wt.% (Fig. 7e) and crystals have average Mg# and Al/Si values of 70 and 0.34, respectively.

Evaluation of amphibole substitution mechanisms based on atomic compositions helps identify changes in crystallization conditions for these phenocrysts, including the pressure-sensitive Al-Tschermak substitution ($2Si^{IV} + Mg^{VI} = 2Al^{IV} + Al^{VI}$) (Johnson & Rutherford, 1989; Thomas & Ernst, 1990; Schmidt, 1992) and temperature-sensitive edenite ($Si^{IV} + \square^{A} = Al^{IV} + (Na + K)^{A}$) and Ti-Tschermak ($2Si^{IV} + Mn^{VI} = 2Al^{IV} + Ti^{VI}$) exchanges (Spear, 1981; Blundy & Holland, 1990) (Fig. 13). Some units show modest changes in Al^{IV} a.p.f.u. (atoms per formula unit) with increasing Al^{VI} a.p.f.u. (Fig. 13a), but many show flat trends indicative of isobaric crystallization of the amphibole with an average Al^{IV} value of 1.75 a.p.f.u. However, amphibole record crystallization over a range of temperatures with evidence for both the edenite and Ti-Tschermak exchanges through increasing $(Na + K)^{A}$ and Ti with increasing Al^{IV} a.p.f.u. (Fig. 13b-c). The relative importance of each mechanism differs between units, where units such as *A* or **LR** exhibit a steep trend for edenite exchange and a shallow trend for Ti-Tschermak exchange, and units like **PI** show the reverse.

Amphibole thermobarometry Amphibole-only and amphibole-liquid thermometry and barometry are applied to estimate temperatures and pressures of Pacheco stage magmas. Temperatures estimated from amphibole-only thermometry for each unit, using Ridolfi & Renzulli (2012), Ridolfi (2021), and Putirka (2016), agree within uncertainty, and each unit records temperatures of ~950–1000°C. We prefer amphibole-liquid temperatures estimated using the lower silica glass for bimodal eruptions, as they are consistent with amphibole-only temperatures for each unit (results shown in Fig. 12c). Amphibole-only pressures using the equations of Ridolfi (2021) consistently record 400–600 MPa, while amphibole-liquid pressures using Putirka's (2016) equations 7a-c record a larger but similar range of 300–600 MPa (results of equation 7a shown in Fig. 12c). Average amphibole-liquid pressures estimated by each equation are identical within uncertainty. We found average temperatures for amphibole with and without reaction rims in a given unit were within expected uncertainty of one another (Electronic Appendix 6).

Amphibole reaction rim significance Observed amphibole textures indicate these magmas experienced variable conditions before eruption. For example, zoned crystals indicate growth in differing magma compositions, while rounded and embayed crystals indicate possible resorption or dissolution related to variable magma heating (Rutherford & Devine, 2003). Amphibole reaction rims are present in five Pacheco stage deposits, four of which contain evidence of magma mingling (**SS**, **LR**, **2K,** and **M**) and one of hybridization (*A*). Reacted amphibole represent up to half but never all of amphibole in a deposit. When present, reaction rims are only found where crystals are in contact with the melt and indicate the importance of melt in their formation (Rutherford & Hill, 1993; Browne & Gardner, 2006). Rims are typically ∼50 μm thick but are up to ∼100 μm in **LR**, and there is a small population of crystals with <25-μm-thick rims. Reaction rims of this type (e.g. Fig. 8l), similar to those found in Misti's **2K** (Tepley III *et al.*, 2013) and sample MIS-99-10b of Ruprecht & Wörner (2007), are often interpreted to result from magma decompression and volatile loss during storage at shallow pressures (e.g. Rutherford & Hill, 1993; Rutherford & Devine, 2003). Heating can also produce reaction rims on amphibole, but Misti's amphibole lack the coarse pyroxene in rims that are consistent with heating (Rutherford & Devine, 2003). High-Al (averages of Al/Si = 0.34 and Al^{IV} = 1.75 a.p.f.u.) regardless of which melt hosts the amphibole, higher percentages of reaction rims on felsic-hosted amphibole, plus constant amphibole-only and amphibole-liquid pressures of ∼300–600 MPa and temperatures of ∼950–1000°C are all consistent with crystallization in a relatively hot intermediate magma at depth (e.g. Kiss *et al.*, 2014). These textures can form from magma simply stalling in the conduit prior to eruption; however, coexistence of reacted and unreacted amphibole within a sample (e.g. Fig. 4e-f) requires a batch of magma to ascend and decompress long enough for rims to form, followed by an additional pulse of magma that mixes with the first and erupts prior to reaction rim formation. The presence of amphibole with and without reaction rims within the same sample in **2K** is interpreted to result from an initial recharge magma pulse into a felsic magma that stagnated above the amphibole stability zone for 50–60 days during which the rims formed. This was followed by a second, more forceful pulse of recharge that hosted unreacted amphibole and mingled with the resident felsic magma body for less than five days before it erupted (Tepley III *et al.*, 2013). Based on similarities in amphibole textures in other units, we deduce similar processes occurred in the remaining mingled deposits with multiple amphibole textural populations. Consequently, we can constrain the storage depth of the felsic magma which, despite being water saturated (Tepley III *et al.*, 2013), must lie outside the stability field for observed amphibole. Experiments on Chilean Andes dacites (Costa *et al.*, 2003; First *et al.*, 2021) and Soufrière Hills andesite (Rutherford & Devine, 2003) suggest that at temperatures >920–950°C, amphibole are unstable at ≤200 MPa, which places an approximate upper limit on storage pressures for Pacheco stage felsic magmas, similar to Tepley III *et al.* (2013). The lack of reaction rims on amphibole crystals in the remaining tephra-fall deposits indicates these magmas made their way to the surface from depth too quickly to dehydrate (e.g. Rutherford & Devine, 2003).

In summary, the following observations suggest that amphibole originated in a broadly intermediate magma at depth:

(1) There is a constant range of amphibole compositions (Al_2O_3 = ∼11–14 wt.%, Al/Si = 0.34, Al^{IV} = 1.75 a.p.f.u.), including the narrow range of rare earth element compositions documented in **2K** regardless of whether the amphibole are reacted or unreacted or hosted in felsic or intermediate glass (Tepley III *et al.*, 2013).
(2) Reacted amphibole are commonly hosted in felsic glass.
(3) There is a dearth of low-Al amphibole that would suggest crystallization in a felsic host (e.g. Kiss *et al.*, 2014).
(4) Amphibole-only and amphibole-liquid estimations steadily record relatively hot (∼950–1000°C) magma temperatures and pressures of ∼300–600 MPa, consistent with experimental phase equilibria estimates.

Clinopyroxene and orthopyroxene

Clinopyroxene and orthopyroxene exist in every unit as a narrow range of augite and enstatite compositions, respectively, with Mg# from 67–84 (Fig. 7d). They appear frequently as single phenocrysts, often with oxide inclusions, or within glomerocrysts of orthopyroxene + clinopyroxene + Fe-Ti oxides ± plagioclase ± amphibole. Phenocrysts are euhedral-subhedral with a subordinate number of anhedral crystals and are unzoned, normally zoned, and reversely zoned. Zoning is commonly marked by diffuse boundaries but sharp zoning contacts are not uncommon. Where pyroxenes are hosted in $\mathbf{SI_R}$ and $\mathbf{SS_{DR}}$, crystals or pyroxene-bearing glomerocrysts are anhedral, resorbed, and generally finer grained than intermediate-hosted counterparts (Fig. 4c-d). We interpret these pyroxenes to have originated in the intermediate magma as glomerocrysts and phenocrysts that then disaggregated and reacted upon mingling and mixing, as documented in other systems (e.g. Bacon & Metz, 1984; Clynne, 1999; Ruprecht *et al.*, 2012). Touching clinopyroxene-orthopyroxene pairs exist in all units except for *A* and **2K**, where crystals are found only as microphenocrysts and microlites comprising ≤1% volume of the samples. Consequently, augite and enstatite compositions of *A* and **2K** exhibit the most compositional diversity with respect to the other Pacheco stage pyroxenes, which are indistinguishable on a Wo-Es-Fs quadrilateral (Fig. 9c).

Pyroxene thermobarometry Two-pyroxene (Putirka, 2008) and clinopyroxene-only (Wang *et al.*, 2021) thermobarometric equations are applied to pyroxenes from each eruption to estimate pressures and temperatures at which they were stored. Average temperatures calculated by two-pyroxene and clinopyroxene-only thermometry are within uncertainty of each other (Fig. 12c), ranging from ∼1000–1100°C for most units, though average clinopyroxene-only temperatures are consistently closer to 1100°C. Although uncertainties are large, two-pyroxene (±280 MPa) and clinopyroxene-only (±160 MPa) barometry consistently produced average pressures of ∼300–500 MPa for all units (Fig. 12b). Values of **2K** magmas record the lowest two-pyroxene and clinopyroxene-only temperatures of ∼925 and ∼ 1000°C, respectively, and the lowest pressures (∼0–200 MPa).

We interpret these observations and thermobarometry estimations to imply the following about pyroxene formation:

(1) High temperatures (≤1100°C) and moderate Mg# (average of 76) are consistent with crystallization in mafic to intermediate magmas. Crystals recording the highest Mg# (up to Mg# 84) may be remnants of recharge and hybridization with more mafic melts, especially since their host whole-rock Mg#s are moderate (Mg# 45–52).
(2) Temperatures and pressures of pyroxene formation remained relatively constant in all but **2K**, which recorded cooler temperatures and lower pressures.
(3) Pressures of pyroxene crystallization fall over a similar interval of amphibole crystallization in the upper crust,

suggesting 300–600 MPa is a major zone of intermediate magma storage and crystallization prior to eruption.

(4) Normal and reverse zoning in pyroxene phenocrysts suggest their involvement in previous episodes of magma mixing.

Fe-Ti oxides

Ilmenite and titanomagnetite occur with a modal abundance of ≤1% as microlites or microphenocrysts, or form inclusions in or are associated with amphibole, pyroxene, plagioclase, and glomerocrysts. Ilmenite and titanomagnetite form touching pairs in all Pacheco stage units, although they are rare in **PI** and *PG*. Additionally, all oxides are texturally homogeneous except for a population in **M**, which display exsolution features. Such crystals are in disequilibrium and not utilized for thermometry or oxygen barometry. In units with bimodal glass compositions, touching pairs are predominantly (sometimes solely) hosted in the higher silica magma.

Fe-Ti oxide thermometry Fe-Ti oxide thermometry and oxygen fugacity estimates presented here use the method of Ghiorso & Evans (2008), using only those pairs in equilibrium based on the test of Bacon & Hirschmann (1988). Pairs record average temperatures of ∼1000–1025°C except for in *A*, **LR**, and **2K** which record cooler temperatures of 943, 907, and 816°C, respectively. Variability in the range of individual estimates is encompassed by the expected uncertainty of the mean except for in *S*, *AP*, and **M** (Fig. 13d). Application of the oxygen barometer of Ghiorso & Evans (2008) yields oxygen fugacities from NNO + 0.9–1.6.

In Pacheco stage deposits with bimodal glass compositions, Fe-Ti oxide pairs are primarily hosted in the felsic melt, and in some cases, ilmenite is absent from the intermediate melt. In **2K**, Fe-Ti oxides record a typical temperature for felsic magma of 816°C, whereas pairs in **SI** and **SS** record 993–1018°C, which are akin to other estimates for the intermediate magmas. Fe-Ti oxide pairs utilized in calculations are texturally and chemically homogenous, implying they either have had no chance to equilibrate with new post-recharge conditions, or they have equilibrated completely. Experiments suggest Fe-Ti oxides re-equilibrate in days to weeks (Gardner *et al.*, 1995; Venezky & Rutherford, 1997, 1999; Hou *et al.*, 2021), and as such, we suggest Fe-Ti oxide temperatures represent the thermal states of Misti's mingled and hybridized magmas just prior to eruption. The occurrence of magma mingling versus hybridization depends on proportions of interacting magmas and their viscosity contrasts, which are controlled by a complex relationship between magma crystallinity, temperature, and volatiles, all of which evolve through time over the mixing process (e.g. Ruprecht *et al.*, 2012). However, as a first order estimate here we use the inferred proportions of disparate magma compositions and their coincident temperatures to support our interpretation. Fe-Ti oxide temperatures of a mixed magma are a function of the original temperatures, fO_2, crystal size, equilibration kinetics, and the time since mixing initiated (e.g. Venezky & Rutherford, 1997). We infer the intermediate magmas in **SI** and **SS** vastly overwhelm the felsic magmas in volume since we observe ≤2% of the felsic melt and a lack of intermediate enclaves in these eruptions. Although the dynamics of mingling will evolve through time after the initial recharge event, heat from the intermediate magmas (∼1000°C) will dominate interaction with a relatively minor cool magma (∼800°C). As such, thermal equilibration of this mixture should correspond to a generally hotter temperature, as is recorded by these deposits (993–1018°C). In contrast, subequal amounts of interacting magmas favor the formation of banding due to development of similar viscosities (Bacon, 1986; Sparks & Marshall, 1986), as is observed in **2K**. If this is the case, the **2K** magma mixture contains proportionally more of the cool silicic magma, which should correspond to an overall cooler temperature, as we observe (816°C). Additionally, time needed for Fe-Ti oxide equilibration to occur (hours to days) is consistent with the timescale of amphibole reaction rim formation upon mixing (days to weeks).

In all, Fe-Ti oxides in the Pacheco stage:

(1) Record the widest range of temperatures among all geothermometers reported herein, from 816°C to 1043°C, which indicate equilibration over a wide range of magma conditions in hours to days following mixing.

(2) Represent the thermal state of mixed magmas prior to eruption, based on inferred proportions of intermediate and felsic magmas and due to rapid Fe-Ti oxide equilibration to new temperatures.

Olivine

Only eight olivine crystals are identified, seven of which are hosted in **PI** and one in *S*. **PI**-hosted olivine are subhedral-anhedral microlites ranging from $Fo_{79–80}$ and are sometimes intergrown with subhedral-anhedral clinopyroxene. *S* hosts a 200-μm anhedral olivine (Fo_{77}) mantled by largely euhedral clinopyroxene and orthopyroxene with wormy intergrowths of Fe-Ti oxides. $Fo_{77–80}$ compositions, disequilibrium textures, and rarity provide additional cryptic evidence of a relatively mafic magma (Zone 3) that interacts and hybridizes with more evolved magmas beneath Misti with which they are no longer in equilibrium.

Glomerocrysts

Crystal aggregates, or glomerocrysts, are common within all Pacheco stage units. They are monomineralic or polymineralic and display a range of assemblages with different combinations of plagioclase, two-pyroxenes, amphibole, and Fe-Ti oxides. Monomineralic glomerocrysts are commonly defined by plagioclase and rarely amphibole, while the most common polymineralic glomerocrysts are plagioclase + two-pyroxenes + Fe-Ti oxides ± amphibole or two-pyroxenes + Fe-Ti oxides. Some glomerocrysts have pockets of interstitial melt and rarely a thin melt film separating crystals. Plagioclase within the clusters are typically moderate-An crystals, although a few high-An cores are present.

Textural relations between crystal clusters and groundmass indicate that these are not xenolith fragments; crystal margins, rather than broken edges, protrude into the groundmass. These glomerocrysts are inferred to represent relics of crystal mats or crystalline mushes produced by crystal settling that were subsequently remobilized by magma recharge pulses and entrained into the new magma (e.g. Seaman, 2000; Cashman *et al.*, 2017; Samaniego *et al.*, 2020). Since plagioclase in clusters with two-pyroxenes or amphibole fall largely in the moderate-An group, and we interpret pyroxene and amphibole to be largely cognate to the intermediate magmas, these common glomerocrysts likely represent crystal settling and accumulation on chamber margins where intermediate magmas are stored. Due to the range of glomerocryst assemblages, we also infer that there is consequential heterogeneity in the magmas stored here. These may represent pulses of magma or spatially disconnected pockets of magma that share similar sources and processes but have all undergone separate thermal and crystallization histories (Eichelberger *et al.*, 2006).

SYNTHESIS OF PETROCHEMICAL DATA

Elucidating three magma storage zones and compositional ranges

We now synthesize the above textural and geochemical observations and thermobarometry to elucidate an understanding of Misti's magmas and their storage system before and during eruption and emplacement of Pacheco stage deposits. We identify three zones (Magma Zones 1–3) which host broadly felsic, intermediate, and mafic magmas, respectively (Fig. 14).

Magma zone 1

Magma Zone 1 is the shallowest zone that stores felsic magma compositions found in $\mathbf{SI_R}$, $\mathbf{SS_{DR}}$, $\mathbf{LR_R}$, $\mathbf{M_{R1}}$, $\mathbf{M_{R2}}$, and $\mathbf{2K_R}$, which appear to be transient and of minimal volume. Felsic magmas likely crystallize plagioclase type III, as these crystals contain the lowest Mg and Fe concentrations and broadly fall along the cool felsic magma equilibrium crystallization trend (Fig. 10a-b). Plagioclase-liquid temperatures employing felsic glasses are variable but consistently cooler (~800–925°C) than those calculated with intermediate glasses (up to ~1000°C). When present, type III plagioclase rarely occur as individual phenocrysts, suggesting they are commonly resorbed by hotter intermediate magmas and the volume of their felsic host is low. Pyroxene record high temperatures (~1000–1100°C) and moderate-high Mg# (67–84), and $\mathbf{SI_R}$- and $\mathbf{SS_{DR}}$-hosted pyroxene are anhedral and sometimes reacted (Fig. 4a-d). These features are inconsistent with crystallization in a felsic host, and it is thus unlikely that pyroxene originated in Magma Zone 1. Although amphibole is sometimes felsic-hosted, they are also unlikely to have crystallized in felsic magmas based on Al contents. Amphibole attributed to dacite and rhyolite magmas elsewhere in Peru are low-Al (<8–10 wt.% Al_2O_3), such as at Tutupaca volcano (Manrique *et al.*, 2020) or the Yanacocha volcanics (Chambefort *et al.*, 2013). Pacheco stage amphiboles' high-Al (>10 wt.% Al_2O_3) coupled with moderate-high Mg# (58–77) support crystallization in a less evolved magma (Kiss *et al.*, 2014). Furthermore, felsic-hosted amphibole at Misti commonly contain fine-grained reaction rims (**LR** and **2K**; e.g. Fig. 7l) or are completely reacted (perhaps **SI**). Because we infer amphibole are cognate to intermediate Zone 2 magmas (discussed below), and felsic-hosted amphibole crystals are often reacted, we can estimate the felsic magma's storage depth. Amphibole reaction rims like those observed in the Pacheco stage has been ascribed to decompression as amphibole ascends, becomes unstable, and reacts with surrounding melt due to the decrease of dissolved water (Browne & Gardner, 2006). Experiments for Volcán San Pedro in the CVZ indicate ≥4 wt.% H_2O is necessary to stabilize amphibole (Costa *et al.*, 2004). With 5 to 6 wt.% H_2O inferred for Misti's magmas (Ruprecht & Wörner, 2007; Tepley III *et al.*, 2013), amphibole should crystallize at appropriate P–T conditions. Experiments discussed above (Costa *et al.*, 2003; Rutherford & Devine, 2003; First *et al.*, 2021) indicate that amphibole at temperatures recorded in the Pacheco stage are unstable at ≤200 MPa. Average amphibole-only and amphibole-liquid barometry estimates from this study indicate Misti's amphibole are stored between 300 and 600 MPa. These phase-equilibria results, combined with details of reaction rim formation support that the magmas in Magma Zone 1 must be shallower than where amphibole are in equilibrium in the magma storage system.

Magma zone 2

Intermediate magmas are the most voluminous, represented by andesitic-dacitic liquids and an assemblage of plagioclase + amphibole + two-pyroxenes + Fe-Ti oxides. We infer the dominant moderate-An plagioclase population (type II) crystallized from these magmas. Consistent pargasitic compositions combined with Al_2O_3 contents of ~11 to 14 wt.% suggest amphibole originated in an intermediate melt. As such, we infer the amphibole are cognate to Zone 2 magmas. Pyroxene also define a narrow range of augite and enstatite compositions, with an average clinopyroxene Mg# of 76. Where pyroxene exist with plagioclase in glomerocrysts, the plagioclase tend to fall in the moderate An-group. Since we ascribe the pyroxene and amphibole to the intermediate magmas, we use two-pyroxene, clinopyroxene-only, amphibole-liquid, and amphibole-only thermobarometry to describe Zone 2 magma storage. Although variability exists, temperatures and pressures garnered from independent methods agree together remarkably well. As such, we estimate the primary zone of intermediate magma storage and crystallization to be at 300–600 MPa with ~950–1000°C magmas (Fig. 11), consistent with phase-equilibria experiments discussed above and two-pyroxene and amphibole-only temperatures from Rivera *et al.* (2017) of 965 ± 45 and 951 ± 33°C, respectively. Pressure- and temperature-sensitive exchange mechanisms evidenced in amphibole compositions (Fig. 12) also indicate polybaric and polythermal crystallization, which are consistent with the range of individual pressure and temperature estimates for intermediate Zone 2 magmas.

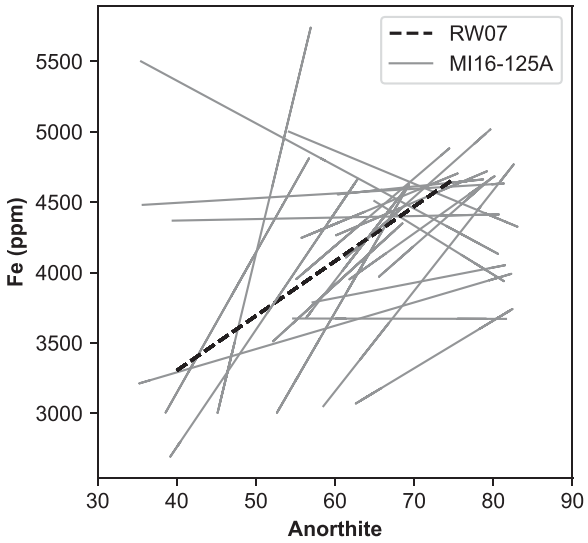

Fig. 11. Plot of best fit lines of anorthite (An) versus Fe (ppm) for individual transect analyses from **LR** sample MI16-125A (solid lines). The 'slightly positive' An-Fe case (dashed line, RW07) from Ruprecht & Wörner (2007) illustrates the maximum An-Fe slope expected from variability in oxygen fugacity at Misti volcano. Note the subset of transects with slopes steeper than that shown by RW07, which necessitates the involvement of distinct magma compositions.

Magma zone 3

Magma Zone 3 is the most enigmatic storage zone. We suggest type I high-An plagioclase and rare olivine ($Fo_{77–80}$) represent the remnants of a cryptic magma antecedent to Zone 2 magmas. We infer these plagioclase and olivine originally crystallized from a hotter, more mafic melt than is otherwise recorded. An-Fe systematics of high-An plagioclase (Fig. 10) suggest growth in a magma with higher Fe than the intermediate melt equilibrium line indicates. Global An-Mg systematics at $>An_{60}$ follow the negative slope of the equilibrium lines, signaling time has passed to allow

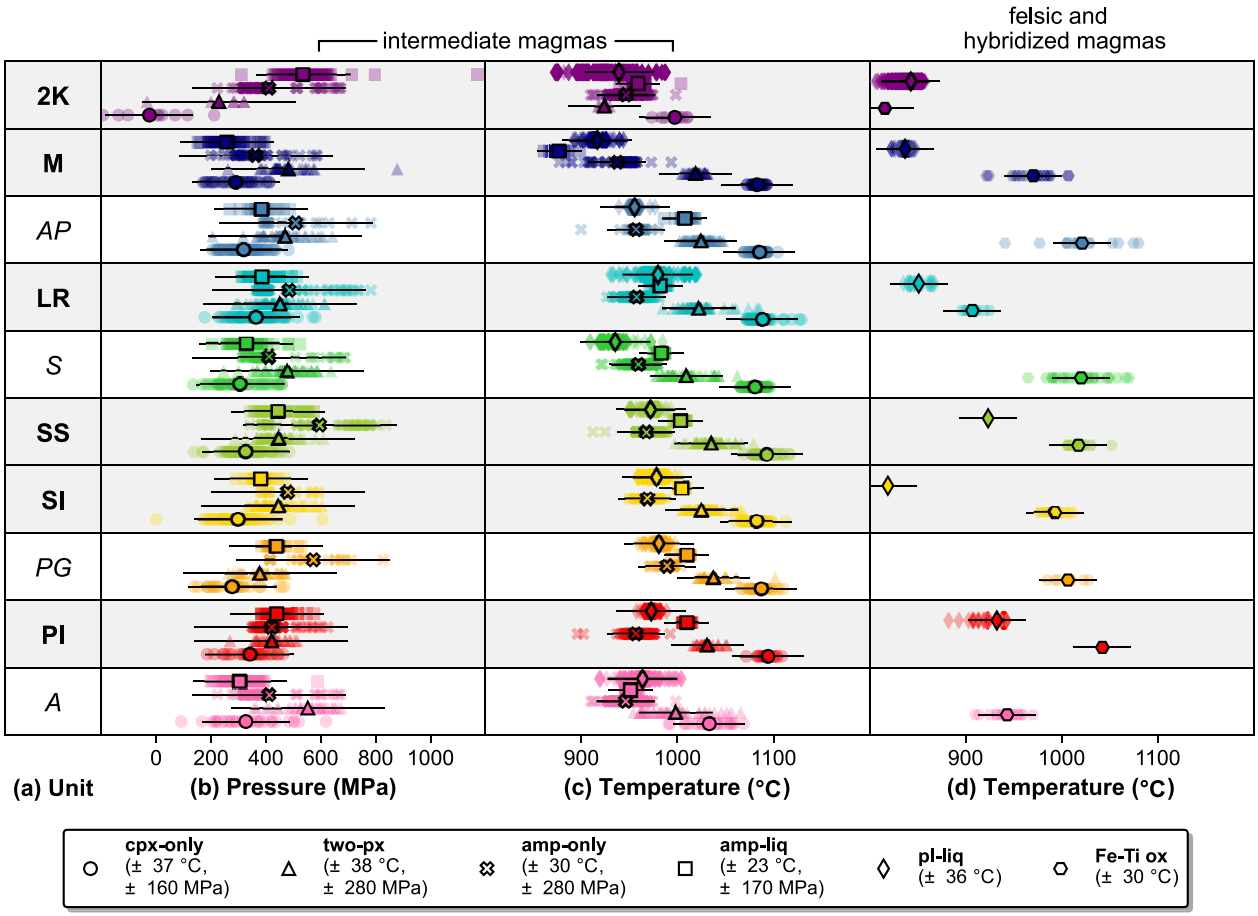

Fig. 12. Summary diagram of all pressures and temperatures estimated via thermobarometry methods outlined in the text. Transparent symbols represent individual data, whereas outlined symbols show average values with expected uncertainties according to the method. Data from Tepley III *et al.* (2013) are used for **2K** estimates. See Electronic Appendix 6 for supplemental information on calculation decisions. (a) Schematic stratigraphic column as in Fig. 7. (b) Pressure estimates from clinopyroxene-only (cpx-only), two-pyroxene (two-px), amphibole-only (amp-only), and amphibole-liquid (amp-liq) barometers. Since we ascribe these phases to intermediate Zone 2 magmas, we suggest that these pressures only represent Misti's intermediate magmas. (c) Temperature estimates from clinopyroxene-only, two-pyroxene, amphibole-only, amphibole-liquid, and plagioclase-liquid (pl-liq) thermometers. For units with bimodal glass compositions, glass with lower silica is used as the liquid in plagioclase-liquid calculations. Similar to pressure estimates, we suggest that these temperatures only represent intermediate Zone 2 magmas. (d) Temperature estimates based on plagioclase-liquid and Fe-Ti oxide (Fe-Ti ox) pairs. Plagioclase-liquid temperatures here are shown for units with bimodal glass compositions and the glass with higher silica is used as the liquid. We contend these plagioclase-liquid temperatures generally represent felsic Zone 1 magmas. Finally, Fe-Ti oxide temperatures represent the thermal state of the mixed magmas shortly prior to eruption, as Fe-Ti oxide pairs equilibrate quickly to new conditions.

for some Mg equilibration via diffusion between injection of high-An crystals, overgrowth of zones with lower An, and eruption. However, individual transects (not plotted here) show not all crystals have reached diffusive equilibrium with Mg. Plagioclase cores with similar sieve textures and compositions ($An_{82–84}$) are found in dacites and andesites identical to those found in quenched basaltic inclusions at Volcán San Pedro, which Costa & Singer (2002) interpreted to be remnants of mechanically disaggregated basaltic xenoliths. Pacheco stage olivine are exceedingly sparse and resorbed crystal forms indicate they are no longer stable in the host melts with which they erupted, and Fo contents are consistent with melts derived from the lower crust. However, as there are no basalt-basaltic andesite glasses documented or mafic xenoliths present, we suggest there is efficient dispersal of mafic recharge magmas into Zone 2 and subsequent hybridization with host melts. The exclusivity of type I plagioclase to cores also indicates that mafic melts are not present at higher levels in the crust. Zoned pyroxene and amphibole, including crystals with the highest Mg#, may also originate in these mafic magmas.

Magma recharge and mixing dynamics (≤21–2 ka)

In volcanic deposits where mixing via recharge or rejuvenation is prominently recorded, it is challenging to resolve what features, if any, represent the magmas prior to mixing and what is the result of mixing. Primitive eruptive products at Misti are lacking, owing to the amount of processing magmas undergo ascending through exceptionally thick crust defining the CVZ (≤75 km; Ryan *et al.*, 2016). Dominant whole-rock compositions during Pacheco stage are andesites (Fig. 5) with Mg# from 45–52, which imply some degree of differentiation (hybridization, assimilation, and/or fractional crystallization) has already occurred previously in the magmas (Barreiro & Clark, 1984; Boily *et al.*, 1990; Thouret *et al.*, 2001; Delacour *et al.*, 2007; Ruprecht & Wörner, 2007; Rivera *et al.*, 2017; Wörner *et al.*, 2018). Superimposed on this protracted history of differentiation is evidence for recent mixing processes recorded in Pacheco stage magmas at various levels in the magma storage system.

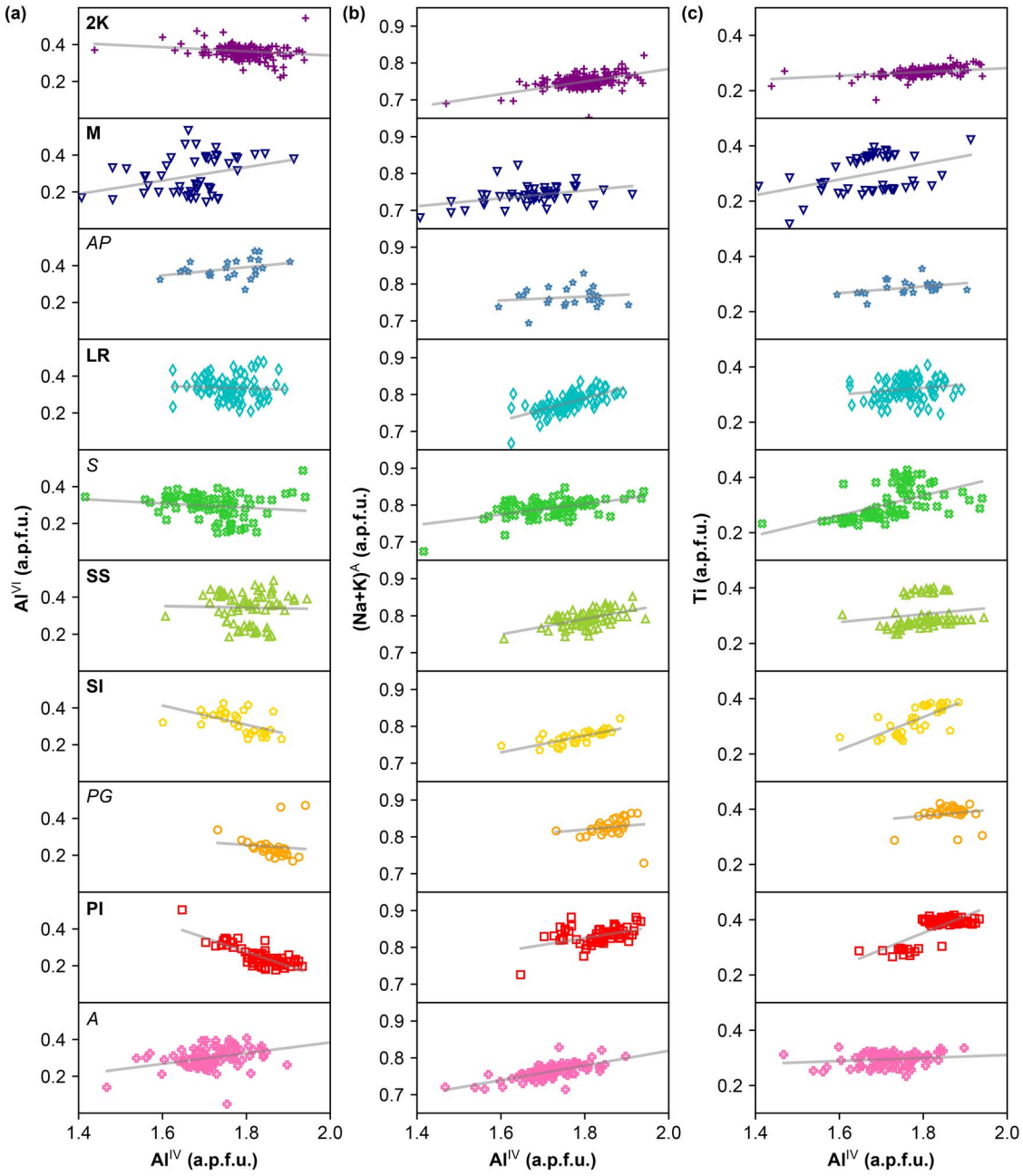

Fig. 13. Amphibole atomic compositions in atoms per formula unit (a.p.f.u.) with best fit lines plotted to highlight relative slopes of trends. The pressure sensitive Al-Tschermak exchange is approximated by (a) Al^{IV} versus Al^{VI}, which shows a variety of trends. Some units show constant Al^{VI} with increasing Al^{IV} indicating isobaric crystallization, while others show decreasing Al^{VI} with increasing Al^{IV} indicating polybaric crystallization. All units show different degrees of temperature-sensitive edenite (b) and Ti-Tschermak (c) exchanges, which highlight the general importance of amphibole crystallization under polythermal conditions. However, thermobarometry estimates herein suggest the ranges of temperatures and pressures of crystallization are limited.

Configuration of magma storage

We suggest the general configuration of Misti's magma storage system during emplacement of explosive Pacheco stage deposits is similar to that proposed by Tepley III *et al.* (2013) based on **2K**. Thermobarometry estimates and phenocryst assemblages and characteristics are consistent with a thermally and chemically stratified magma storage system (Fig. 14). Associations between magmas recorded in tephra indicate Misti's system is zoned with increasing evolution as depth decreases (e.g. Cashman *et al.*, 2017). Although there is no direct barometric estimate for Zone 3, the observations that mafic liquids are absent in tephra and there is no growth of high-An plagioclase on moderate- or low-An crystals indicate it is stored below Zone 1–2 magmas. Evidence for the existence of mafic magmas is preserved as mafic antecrysts, but the mafic magmas themselves are filtered and diluted before eruption. The variety and complexity of glomerocrysts cognate to the intermediate magmas signal significant textural heterogeneity among them. If there is a single large intermediate reservoir (Ruprecht & Wörner, 2007), we envision a varied crystal mush heterogeneously sampled during different eruptions (e.g. Wörner *et al.*, 2018; Samaniego *et al.*, 2020). These features could alternatively be explained by a plexus of dikes and sills, where

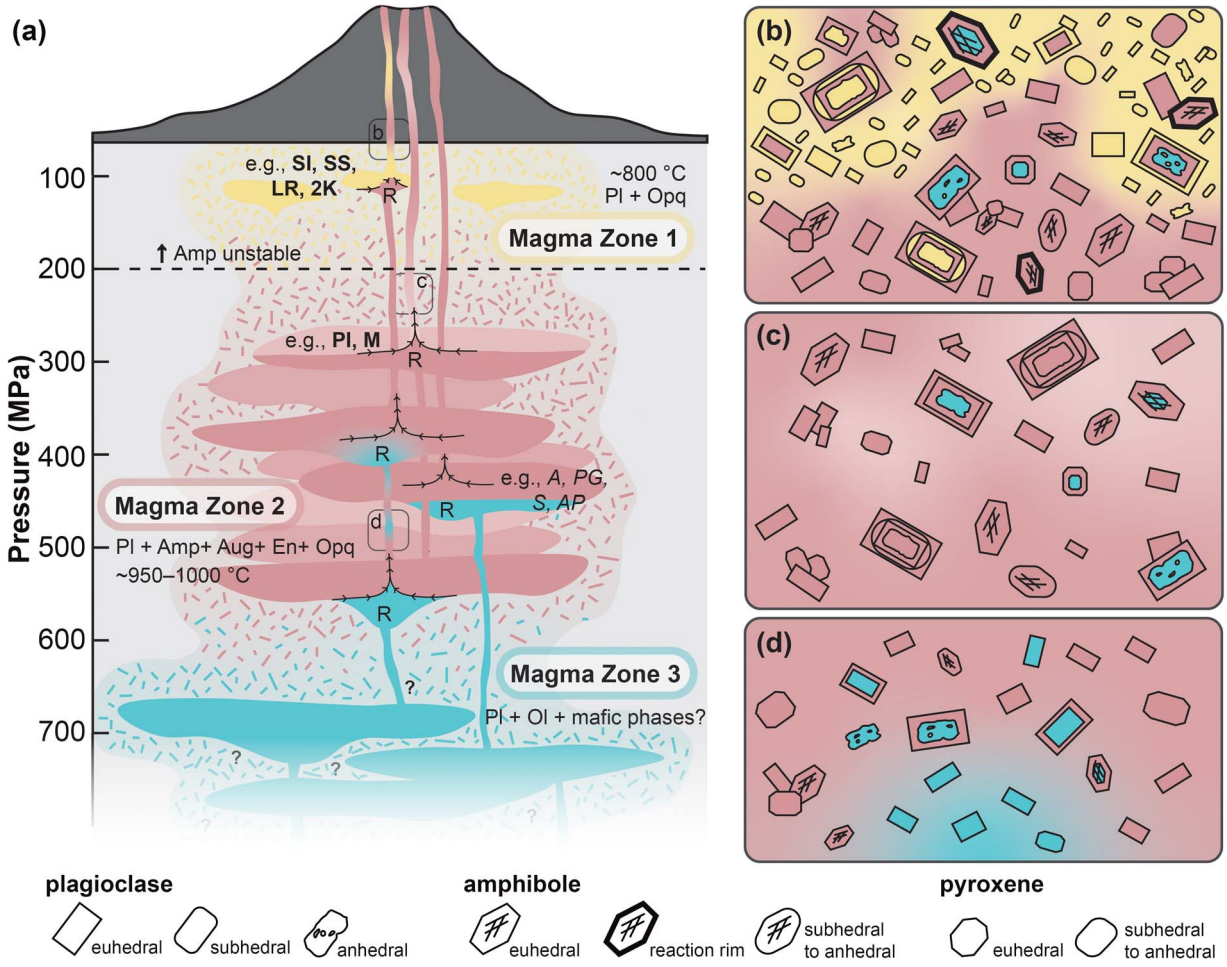

Fig. 14. Simplified representation of Misti volcano's magma storage system and processes that account for petrological features of Pacheco stage explosive deposits. Physical features not to scale. (a) Magmas exist in three zones: Zone 1, shallow (≤200 MPa), cool (~800°C), and broadly silicic magmas crystallizing low-An (anorthite) plagioclase (Pl) + Fe-Ti oxides (Opq); Zone 2, broadly intermediate magmas residing at ~300–600 MPa and ~950–1000°C with moderate-An plagioclase + amphibole (Amp) + two-pyroxenes (Aug and En) + Fe-Ti oxides; and Zone 3, broadly mafic magmas staged deeper relative to Zone 2 with at least high-An plagioclase + olivine (Ol) in the phase assemblage. R denotes a recharge event. (b) Melt and mineral textures that result from recharge and mingling between Zone 1 and 2 magmas, with antecrystic cores from Zone 3 magmas. (c) Melt and mineral textures that result from rejuvenation and mingling in the conduit of two broadly similar compositions, resulting in plagioclase with generally similar compositions. Alternatively, this could result from remobilization of a compositionally zoned chamber with a subtle chemical gradient. (d) Melt and mineral textures that result from recharge and mingling between Zone 2 and 3 magmas.

glomerocryst and textural heterogeneity can be generated via unequal storage and cooling histories (e.g. Eichelberger *et al.*, 2006). However, continuously high magma temperatures that suggest the system is thermally buffered and apparently efficient hybridization between mafic and intermediate magmas support some form of a continuous intermediate magma reservoir.

Snapshots of evolving viscosity contrasts

Hybridization is prevented early during mixing by initially high viscosity contrasts, such as those expected between mafic and felsic magmas (Sparks & Marshall, 1986), and the result is mingled magmas frozen upon eruption. As time since mixing increases, magma viscosities evolve with changing crystallinities, water contents, and temperatures, and viscosity contrasts can decrease between the magmas such that hybridization of the melt is promoted (Ruprecht *et al.*, 2012). Although the trend is imperfect, we propose the alternation of tephra with unimodal and bimodal glass compositions (Fig. 7b) provides snapshots of this process as it progresses. For example, we calculate magma viscosities based on glass compositions of **SI**, **SS**, and S using the model of Giordano *et al.* (2008). **SI** records a mingled magma with highly contrasting liquids where initial viscosity contrast between them is high ($\mathbf{SI_A}$, $10^{3.5–3.7}$ Pa s; $\mathbf{SI_R}$, $10^{5.2–5.6}$ Pa s), and eruption must have occurred while the contrast was still relatively high, thus mingling is preserved. **SI** is followed by eruption of **SS**, which is macroscopically indistinguishable from **SI** and contains comparable phenocryst populations overall. However, while most glass compositions still define a bimodal distribution, the most felsic $\mathbf{SS_{DR}}$ glass compositions have comparatively lower silica than $\mathbf{SI_R}$ and a subset of analyses fall in the middle. Compared to initial viscosities of $\mathbf{SI_A}$ and $\mathbf{SI_R}$, heat exchange between the magmas greatly reduces the viscosity of $\mathbf{SS_{DR}}$ ($10^{4.7–5.0}$ Pa s) and raises the viscosity of $\mathbf{SS_{AD}}$ ($10^{3.7–4.2}$ Pa s) slightly. Characteristics of **SS** are consistent with limited hybridization of $\mathbf{SI_A}$ and $\mathbf{SI_R}$ after initial differences in viscosity are reduced, but these magmas erupt before complete hybridization. The next eruption in the sequence is S, which has unimodal glass compositions that fall between $\mathbf{SS_{AD}}$ and $\mathbf{SS_{DR}}$. An intermediate melt viscosity of $10^{4.2–4.5}$ Pa s records the final stage of converging melt viscosities and complete hybridization of the melt followed by eruption.

Changing regimes at Misti

Although the ca. 2-ka eruption is unique in several ways, our analyses of nine explosive eruptions immediately preceding its emplacement reveal it is just the most recent and striking expression of Misti's magma mixing history. Volumetrically, the magmas that supplied Pacheco stage deposits older than the ca. 2-ka eruption are dominated by intermediate magmas with only ≤2% represented by more felsic melts, and more mafic magmas preserved in mafic phases. The Cayma stage, which precedes the Pacheco stage by about 10 ky, emplaced dacitic and rhyolitic tephra-all deposits without obvious involvement of more mafic magmas during eruptions of magnitude VEI ≤5 (Harpel *et al.*, 2023). The Pacheco stage continues to erupt felsic magmas; however, some characteristics are different. While the Cayma stage Sacarosa deposit contains an unreacted hydrous mineral assemblage stored at ~300–400 MPa prior to rapid ascent and eruption (Harpel *et al.*, 2023), we have demonstrated Pacheco stage felsic magmas are comparatively shallow (≤200 MPa). Rather than erupting on their own, Zone 1 magmas are sampled only during recharge by and mixing with deeper intermediate magmas bodies that dominate the magmatic signature. We suggest that because these felsic magmas are cool (~800°C) and low in volume, they are potentially locked up, creating a barrier to eruption. Recharge from hotter Zone 2 magmas (~950–1000°C) serves to remobilize parts of a felsic crystal mush prior to eruption via heating and mechanical processes (Huber *et al.*, 2011). Several observations are consistent with mixing between a high ratio of hot, low viscosity intermediate magmas to cool, high viscosity felsic magmas, such as the lack of intermediate enclaves in felsic tephra (Sparks & Marshall, 1986) as well as the sparsity of felsic tephra. Crystals composed entirely of low-An compositions are exceedingly rare, and they are most commonly found in rims, suggesting a brief late-stage interaction. The inference that low-An plagioclase crystals were largely resorbed is consistent with a significant heating event (i.e. heat input from hot recharge). A high ratio of intermediate to felsic magma is perhaps maintained due to injection via diking into felsic mush that is sufficiently forceful that it erupts without much dispersal into the chamber (e.g. Eichelberger *et al.*, 2006; Walker *et al.*, 2013).

The abrupt transition from eruption of bulk dacites and rhyolites in the Cayma stage (Harpel *et al.*, 2023) to bulk andesites in the Pacheco stage with little interaction with evolved magmas is observed at other volcanoes in the CVZ, such as Parinacota. During Parinacota's 'Old Cone' stage, it produced basaltic andesites and rhyolites and transitioned to uniform mafic andesites after edifice collapse in its 'New Cone' stage (Hora *et al.*, 2007; Wörner *et al.*, 2018). Changes in erupted compositions at Parinacota are thought to be a function of the magma recharge rate. The Old Cone represents an 'activation regime' where increased but variable recharge juxtaposes mafic and felsic magmas that variably mix and erupt, whereas the New Cone represents a 'breakthrough' regime where recharge rates are high and there is limited mixing with older felsic magma batches (Wörner *et al.*, 2018). The Pacheco stage may represent a similar transition to high rates of magma recharge, which is consistent with persistently high magma temperatures (~950–1000°C) and low degrees of interaction with felsic magmas.

Eruption triggers

The importance of magma recharge at Misti has been demonstrated here and in previous investigations (Ruprecht & Wörner, 2007; Tepley III *et al.*, 2013). Magma recharge has long been recognized as an eruption trigger for explosive volcanic eruptions (e.g. Eichelberger, 1974; Anderson, 1976; Sparks *et al.*, 1977). Specific mechanisms related to magma recharge invoked as eruption triggers include the introduction of mass, volatiles, and/or heat from a recharge magma leading to overpressure, remobilization, and/or buoyancy of the resident magma. Mingled glasses present in five tephra-fall deposits out of the last ten explosive eruptions suggests that magma recharge must have occurred shortly before eruption, otherwise evidence of recharge in the melt would have been lost to hybridization. Even rimward analyses of crystals in A indicate that recharge was one of the last incidents recorded. The dearth of felsic and mafic magmas erupting unaccompanied by intermediate magmas is also consistent with recharge filtering (Kent *et al.*, 2010). Andesitic magma formation in the CVZ can be explained by hybridization of mafic and felsic magmas (Anderson, 1976; Eichelberger, 1980; Reubi & Blundy, 2009; Wörner *et al.*, 2018), but the high density of mafic and low viscosity of felsic magmas make them less likely to erupt. However, recharge of a hotter, less viscous, and more mobile mafic magma into a shallower, rheologically locked felsic magma promotes mixing and the petrogenesis of intermediate magmas, which can overcome the barriers to eruption (Kent *et al.*, 2010). That andesites comprise the overwhelming majority of deposits during this time indicate that mafic recharge is a key process occurring at Misti even if it does not lead to an immediate eruption (Ruprecht & Wörner, 2007), and that there is a significant crustal barrier to eruption.

CONCLUSIONS

Geochemical and petrological analyses of ten of Misti's most recent tephra-fall deposits indicate a complex, multi-stage history of magma ascent, storage, and differentiation since ≤21 ka. Glass and mineral compositions and textures, phase equilibria, and thermobarometry estimates indicate a chemically and thermally stratified magma storage system in the form of three distinct magma zones host to broadly mafic, intermediate, and felsic magmas. Remnants of an unerupted mafic magma appear only as antecrystic high-An plagioclase cores, trace olivine, and possibly high Mg# augite and amphibole (up to Mg# 84 and 77, respectively). Intermediate magmas, which we estimate to be stored at ~950–1000°C and 300–600 MPa, dominate Misti's erupted products. Periodically, these intermediate magmas interact with shallow (<200 MPa) and cool (~800°C) felsic magmas that do not erupt alone but may be remobilized and mixed with the intermediate magmas upon recharge. Magma mixing interactions are recorded by glass compositions and crystal exchange, including an apparent alternation between eruption of mingled and hybridized magmas that reflect reductions in viscosity contrasts as time passes between recharge events. This investigation suggests magma recharge is the leading mechanism by which explosive eruptions are triggered at Misti during the Pacheco stage and demonstrates the wealth of critical petrological information to be gleaned by examination of a series of young explosive eruptions at an active and hazardous volcano.

ACKNOWLEDGEMENTS

Assistance with LA-ICP-MS data collection from Chris Russo and data reduction from Jordan Lubbers was greatly appreciated. Many thanks to Kevin Cueva, Nelida Manrique, Juan Jose Cuno, David Valdivia, Marquinho Cabrera, Yhon Soncco, Saida Japura, Jessica Vela, and Gian Marco Escobar for help in the field. We are

sincerely grateful for reviews by John Eichelberger, Matt Loewen, Philipp Ruprecht, Heather Wright, and an anonymous reviewer which helped to strengthen our ideas and greatly improved the readability of this manuscript. Any use of trade, firm, or product names is for descriptive purposes only and does not imply endorsement by the U.S. Government.

FUNDING

This work was supported by a Jack Kleinman Grant for Volcano Research, Geological Society of America Lipman Graduate Student Research Grant, and Mineralogical Society of America Grant for Student Research in Mineralogy and Petrology to M.K.T.; the U.S. Agency for International Development Bureau for Humanitarian Assistance (AID-OFDA-T-12-00001 to C.J.H.), and the Fondo Nacional Científico, Tecnológico y de Innovación Tecnológica del Consejo Nacional de Ciencia, Tecnología e Innovación Tecnológica del Perú (Convenio 158–2017-FONDECYT to R.A. and M.R.).

DATA AVAILABILITY

Supplementary data for this paper are available at *Journal of Petrology* online, including: representative outcrop and tephra photos (Electronic Appendix 1), whole-rock data (Electronic Appendix 2; see also Takach *et al.*, 2024), EMP spot analyses (Electronic Appendix 3; see also Takach *et al.*, 2024), LA-ICP-MS and EMP transects (Electronic Appendix 4), details of analytical analyses (Electronic Appendix 5), and thermobarometry considerations (Electronic Appendix 6).

REFERENCES

Adams, N. K., De Silva, S. L., Self, S., Salas, G., Schubring, S., Permenter, J. L. & Arbesman, K. (2001). The physical volcanology of the 1600 eruption of Huaynaputina, southern Peru. *Bulletin of Volcanology* **62**, 493–518. https://doi.org/10.1007/s004450000105.

Anderson, A. T. (1976). Magma mixing: petrological process and volcanological tool. *Journal of Volcanology and Geothermal Research* **1**, 3–33. https://doi.org/10.1016/0377-0273(76)90016-0.

Anderson, A. T. (1984). Probable relations between plagioclase zoning and magma dynamics, Fuego volcano, Guatemala. *American Mineralogist* **69**, 660–676.

Armienti, P., Tonarini, S., Innocenti, F. & D'Orazio, M. (2007). Mount Etna pyroxene as tracer of petrogenetic processes and dynamics of the feeding system. *Special Paper 418: Cenozoic Volcanism in the Mediterranean Area* **2418**, 265–276.

Asimow, P. D. & Ghiorso, M. S. (1998). Algorithmic modifications extending MELTS to calculate subsolidus phase relations. *American Mineralogist* **83**, 1127–1132. https://doi.org/10.2138/am-1998-9-1022.

Bacon, C. R. (1986). Magmatic inclusions in silicic and intermediate volcanic rocks. *Journal of Geophysical Research* **91**, 6091–6112. https://doi.org/10.1029/JB091iB06p06091.

Bacon, C. R. & Hirschmann, M. M. (1988). Mg/Mn partitioning as a test for equilibrium between coexisting Fe-Ti oxides. *American Mineralogist* **73**, 57–61.

Bacon, C. R. & Metz, J. (1984). Magmatic inclusions in rhyolites, contaminated basalts, and compositional zonation beneath the Coso volcanic field, California. *Contributions to Mineralogy and Petrology* **85**, 346–365. https://doi.org/10.1007/BF01150292.

Barreiro, B. A. & Clark, A. H. (1984). Lead isotopic evidence for evolutionary changes in magma-crust interaction, Central Andes, southern Peru. *Earth and Planetary Science Letters* **69**, 30–42. https://doi.org/10.1016/0012-821X(84)90072-4.

Bindeman, I. N., Davis, A. M. & Drake, M. J. (1998). Ion microprobe study of plagioclase-basalt partition experiments at natural concentration levels of trace elements. *Geochimica et Cosmochimica Acta* **62**, 1175–1193. https://doi.org/10.1016/S0016-7037(98)00047-7.

Birnie, R. W. & Hall, J. H. (1974). The geochemistry of El Misti volcano, Peru fumaroles. *Bulletin Volcanologique* **38**, 1–15. https://doi.org/10.1007/BF02597797.

Blundy, J. D. & Holland, T. J. (1990). Calcic amphibole equilibria and a new amphibole–plagioclase geothermometer. *Contributions to Mineralogy and Petrology* **104**, 208–224. https://doi.org/10.1007/BF00306444.

Bohrson, W. A., Spera, F. J., Ghiorso, M. S., Brown, G. A., Creamer, J. B. & Mayfield, A. (2014). Thermodynamic model for energy-constrained open-system evolution of crustal magma bodies undergoing simultaneous recharge, assimilation and crystallization: the magma chamber simulator. *Journal of Petrology* **55**, 1685–1717. https://doi.org/10.1093/petrology/egu036.

Bohrson, W. A., Spera, F. J., Heinonen, J. S., Brown, G. A., Scruggs, M. A., Adams, J. V., Takach, M. K., Zeff, G. & Suikkanen, E. (2020). Diagnosing open-system magmatic processes using the magma chamber simulator (MCS): part I—major elements and phase equilibria. *Une chaire de médecine au XVe siècle; un professeur à l'Université de Pavie de 1432 à 1472* **175**, 1–29. https://doi.org/10.1007/s00410-020-01722-z.

Boily, M., Ludden, J. N. & Brooks, C. (1990). Geochemical constraints on the magmatic evolution of the pre- and post-Oligocene volcanic suites of southern Peru: implications for the tectonic evolution of the Central Volcanic Zone. *Geological Society of America Bulletin* **102**, 1565–1579. https://doi.org/10.1130/0016-7606(1990)102<1565:GCOTME>2.3.CO;2.

Bowen, N. L. (1928) *The Evolution of the Igneous Rocks*. Princeton, NJ: Princeton University Press, 104.

Browne, B. L. & Gardner, J. E. (2006). The influence of magma ascent path on the texture, mineralogy, and formation of hornblende reaction rims. *Earth and Planetary Science Letters* **246**, 161–176. https://doi.org/10.1016/j.epsl.2006.05.006.

Cacya, L., Mariño, J., Rivera, M. & Thouret, J.-C. (2007). La Erupción Pliniana "Autopista" del Volcán Misti (21,000-11,000 años AP). *Boletin de la Sociedad Geológica del Perú* **102**, 25–42.

Cashman, K. V., Sparks, R. S. J. & Blundy, J. D. (2017). Vertically extensive and unstable magmatic systems: a unified view of igneous processes. *Science* **355**, 1–9. https://doi.org/10.1126/science.aag3055.

Chambefort, I., Dilles, J. H. & Longo, A. A. (2013). amphibole geochemistry of the Yanacocha Volcanics, Peru: evidence for diverse sources of magmatic volatiles related to gold ores. *Journal of Petrology* **54**, 1017–1046. https://doi.org/10.1093/petrology/egt004.

Chávez Chávez, J. A. (1992) *La erupción del volcán Misti*. Arequipa: Impresiones Zenit.

Clynne, M. A. (1999). A complex magma mixing origin for rocks erupted in 1915, Lassen Peak, California. *Journal of Petrology* **40**, 105–132. https://doi.org/10.1093/petroj/40.1.105.

Cobeñas, G., Thouret, J.-C., Bonadonna, C. & Boivin, P. (2012). The c.2030 yr BP Plinian eruption of El Misti volcano, Peru: eruption dynamics and hazard implications. *Journal of Volcanology and Geothermal Research* **241–242**, 105–120.

Conrey, R. M., Bailey, D. G., Singer, J. W., Wagoner, L. J., Parfitt, B., Hay, J., Keh, O., Chang, Z. & Huang, S. (2019). Combined use of multiple

internal and external standards in LA-ICP-MS analysis of bulk geological amples using lithium borate fused glass. *Geochemistry: Exploration, Environment, Analysis* **23**, 1–16.

Costa, F. & Singer, B. (2002). Evolution of Holocene dacite and compositionally zoned magma, Volcán San Pedro, Southern Volcanic Zone, Chile. *Journal of Petrology* **43**, 1571–1593. https://doi.org/10.1093/petrology/43.8.1571.

Costa, F., Chakraborty, S. & Dohmen, R. (2003). Diffusion coupling between trace and major elements and a model for calculation of magma residence times using plagioclase. *Geochimica et Cosmochimica Acta* **67**, 2189–2200. https://doi.org/10.1016/S0016-7037(02)01345-5.

Costa, F., Scaillet, B. & Pichavant, M. (2004). Petrological and experimental constraints on the pre-eruption conditions of Holocene dacite from Volcán San Pedro (36°S, Chilean Andes) and the importance of sulphur in silicic subduction-related magmas. *Journal of Petrology* **45**, 855–881. https://doi.org/10.1093/petrology/egg114.

Couch, S., Sparks, R. S. J. & Carroll, M. R. (2001). Mineral disequilibrium in lavas explained by convective self-mixing in open magma chambers. *Nature* **411**, 1037–1039. https://doi.org/10.1038/35082540.

Cuno, J. J. (2018) *Estudio de la erupción del volcán Misti occurida hace 33,7 mil años AP, que emplazo el depósito "Sacarosa" en la ciudad de Arequipa*. Ingeniero Thesis. Universidad Nacional de San Agustin de Arequipa.

Davidson, J. P., Harmon, R. S. & Wörner, G. (1991). The source of central Andean magmas; Some considerations. *Geological Society of America Special Paper* **265**, 233–243.

Delacour, A., Gerbe, M. C., Thouret, J.-C., Wörner, G. & Paquereau-Lebti, P. (2007). Magma evolution of quaternary minor volcanic centres in southern Peru, Central Andes. *Bulletin of Volcanology* **69**, 581–608. https://doi.org/10.1007/s00445-006-0096-z.

Deer, W. A., Howie, R. A., & Zussman, J. (1992). *An introduction to the rock-forming minerals*. 2nd ed. Harlow, Essex, England: New York, NY, Longman Scientific & Technical.

Dungan, M. A. & Rhodes, J. M. (1978). Residual glasses and melt inclusions in basalts from DSDP legs 45 and 46: evidence for magma mixing. *Contributions to Mineralogy and Petrology* **67**, 417–431. https://doi.org/10.1007/BF00383301.

Eichelberger, J. C. (1974). Magma contamination within the volcanic pile: origin of andesite and dacite. *Geology* **2**, 29–33. https://doi.org/10.1130/0091-7613(1974)2<29:MCWTVP>2.0.CO;2.

Eichelberger, J. C. (1980). Vesiculation of mafic magma during replenishment of silicic magma reservoirs. *Nature* **288**, 446–450. https://doi.org/10.1038/288446a0.

Eichelberger, J. C., Izbekov, P. E. & Browne, B. L. (2006). Bulk chemical trends at arc volcanoes are not liquid lines of descent. *Lithos* **87**, 135–154. https://doi.org/10.1016/j.lithos.2005.05.006.

Ferlito, C., Viccaro, M. & Cristofolini, R. (2009). Volatile-rich magma injection into the feeding system during the 2001 eruption of Mt. Etna (Italy): its role on explosive activity and change in rheology of lavas. *Bulletin of Volcanology* **71**, 1149–1158. https://doi.org/10.1007/s00445-009-0290-x.

First, E. C., Hammer, J. E., Ruprecht, P. & Rutherford, M. (2021). Experimental constraints on dacite magma storage beneath Volcán Quizapu, Chile. *Journal of Petrology* **62**, 1–26. https://doi.org/10.1093/petrology/egab027.

Gardner, J. E., Carey, S., Rutherford, M. J. & Sigurdsson, H. (1995). Petrologic diversity in Mount St. Helens dacites during the last 4,000 years: implications for magma mixing. *Contributions to Mineralogy and Petrology* **119**, 224–238. https://doi.org/10.1007/BF00307283.

Gerbe, M. C. & Thouret, J.-C. (2004). role of magma mixing in the petrogenesis of tephra erupted during the 1990–98 explosive activity of Nevado Sabancaya, southern Peru. *Bulletin of Volcanology* **66**, 541–561. https://doi.org/10.1007/s00445-004-0340-3.

Gerlach, D. C. & Grove, T. L. (1982). Petrology of Medicine Lake Highland volcanics: characterization of endmembers of magma mixing. *Contributions to Mineralogy and Petrology* **80**, 147–159. https://doi.org/10.1007/BF00374892.

Ghiorso, M. S. & Evans, B. W. (2008). Thermodynamics of rhombohedral oxide solid solutions and a revision of the Fe-Ti two-oxide geothermometer and oxygen-barometer. *American Journal of Science* **308**, 957–1039. https://doi.org/10.2475/09.2008.01.

Ghiorso, M. S. & Gualda, G. A. R. (2015). An H_2O–CO_2 mixed fluid saturation model compatible with rhyolite-MELTS. *Contributions to Mineralogy and Petrology* **169**, 1–30.

Ghiorso, M. S. & Sack, R. O. (1995). Chemical mass transfer in magmatic processes IV. A revised and internally consistent thermodynamic model for the interpolation and extrapolation of liquid–solid equilibria in magmatic systems at elevated temperatures and pressures. *Contributions to Mineralogy and Petrology* **119**, 197–212. https://doi.org/10.1007/BF00307281.

Ghiorso, M. S., Hirschmann, M. M., Reiners, P. W. & Kress, V. C. (2002). The pMELTS: a revision of MELTS for improved calculation of phase relations and major element partitioning related to partial melting of the mantle to 3 GPa. *Geochemistry, Geophysics, Geosystems* **3**, 1–35. https://doi.org/10.1029/2001GC000217.

Ginibre, C. & Wörner, G. (2007). Variable parent magmas and recharge regimes of the Parinacota magma system (N. Chile) revealed by Fe, Mg and Sr zoning in plagioclase. *Lithos* **98**, 118–140. https://doi.org/10.1016/j.lithos.2007.03.004.

Ginibre, C., Kronz, A. & Wörner, G. (2002a). High-resolution quantitative imaging of plagioclase composition using accumulated backscattered electron images: new constraints on oscillatory zoning. *Contributions to Mineralogy and Petrology* **142**, 436–448. https://doi.org/10.1007/s004100100298.

Ginibre, C., Wörner, G. & Kronz, A. (2002b). Minor- and trace-element zoning in plagioclase: implications for magma chamber processes at Parinacota volcano, northern Chile. *Contributions to Mineralogy and Petrology* **143**, 300–315. https://doi.org/10.1007/s00410-002-0351-z.

Ginibre, C., Wörner, G. & Kronz, A. (2007). Crystal zoning as an archive for magma evolution. *Elements* **3**, 261–266. https://doi.org/10.2113/gselements.3.4.261.

Giordano, D., Russel, J. K. & Dingwell, D. B. (2008). Viscosity of magmatic liquids: a model. *Earth and Planetary Science Letters* **271**, 123–134. https://doi.org/10.1016/j.epsl.2008.03.038.

Gualda, G. A. R., Ghiorso, M. S., Lemons, R. V. & Carley, T. L. (2012). Rhyolite-MELTS: a modified calibration of MELTS optimized for Ilica-rich, fluid-bearing magmatic systems. *Journal of Petrology* **53**, 875–890. https://doi.org/10.1093/petrology/egr080.

Hantke, G. & Parodi, A. (1966) *Catalogue of the active volcanoes of the world including Solfatara fields – Part XIX Colombia, Ecuador, and Peru*. Rome: International Association of Volcanology.

Harpel, C. J., de Silva, S. & Salas, G. (2011). The 2 ka eruption of Misti volcano, southern Peru - the most recent Plinian eruption of Arequipa's iconic volcano. *Geological Society of America Special Paper* **484**, 1–72.

Harpel, C. J., Rivera, M., Tepley, F., Cuno, J. J., Manrique, N., Aguilar, R., Cueva, K., Dossey, M. A., Japura, S., Cabrera, M. & Soncco, Y. (2018) Preliminary tephrostratigraphy and eruption history of Misti volcano, southern Peru, since the late Pleistocene. Abstract (V51F-0169) presented at AGU18, 10–14 December.

Harpel, C. J., Aguilar, R., Rivera, M., Tepley, F., Takach, M., Manrique, N., Cuno, J., Cueva, K., Escobar, G. M., Allen, I., Pawlak-Kjolhaug, K., Sankovitch, L., Topham, J. & Lewis, C. (2021) Tephrostratigraphy of Misti Volcano, Arequipa, Peru: A Chronicle of Multiple VEI 2-5 Eruptions from the Late Pleistocene to the Mid-15th Century. Abstract (V45C-0145) presented at AGU21, 13-17 December.

Harpel, C. J., Cuno, J. J., Takach, M. K., Rivera, M., Aguilar, R., Tepley, F. J. & Garcia, F. (2023). The late Pleistocene Sacarosa tephra-fall deposit, Misti volcano, Arequipa, Peru: its magma, eruption, and implications past and future eruptive activity. *Bulletin of Volcanology* **85**, 1–24. https://doi.org/10.1007/s00445-023-01654-z.

Hildreth, W. (1981). Gradients in silicic magma chambers: implications for lithospheric magmatism. *Journal of Geophysical Research* **86**, 10153–10192. https://doi.org/10.1029/JB086iB11p10153.

Hora, J. M., Singer, B. S. & Wörner, G. (2007). Volcano evolution and eruptive flux on the thick crust of the Andean Central Volcanic Zone: $^{40}Ar/^{39}Ar$ constraints from Volcán Parinacota, Chile. *Geological Society of America Bulletin* **119**, 343–362. https://doi.org/10.1130/B25954.1.

Hou, T., Botcharnikov, R., Moulas, E., Just, T., Berndt, J., Koepke, J., Zhang, Z., Wang, M., Yang, Z. & Holtz, F. (2021). Kinetics of Fe-Ti oxide re-equilibration in magmatic systems: implications for thermo-oxybarometry. *Journal of Petrology* **61**, 1–24. https://doi.org/10.1093/petrology/egaa116.

Housh, T. B. & Luhr, J. F. (1991). Plagioclase-melt equilibria in hydrous systems. *American Mineralogist* **76**, 477–492.

Huber, C., Bachmann, O. & Dufek, J. (2011). Thermo-mechanical reactivation of locked crystal mushes: Melting-induced internal fracturing and assimilation processes in magmas. *Earth and Planetary Science Letters* **304**, 443–454.

INEI. (2018). Perú Encuesta Demográfica y de Salud Familiar-ENDES. *Instituto Nacional de Estadística e Informática* (https://www.inei.gob.pe/media/MenuRecursivo/publicaciones_digitales/Est/Lib1656/index1.html).

Johnson, M. C. & Rutherford, M. J. (1989). Experimental calibration of the aluminum-in-hornblende geobarometer with application to Long Valley caldera (California) volcanic rocks. *Geology* **17**, 837–841. https://doi.org/10.1130/0091-7613(1989)017<0837:ECOTAI>2.3.CO;2.

Johnson, D. M., Hooper, P. R. & Conrey, R. M. (1999). XRF analysis of rocks and minerals for major and trace elements on a single low dilution Li-tetraborate fused bead. *Advances in X-Ray Analysis*, 843–867.

Kawamoto, T. (1992). Dusty and honeycomb plagioclase: indicators of processes in the Uchino stratified magma chamber, Izu Peninsula, Japan. *Journal of Volcanology and Geothermal Research* **49**, 191–208. https://doi.org/10.1016/0377-0273(92)90014-5.

Kent, A. J. R., Darr, C., Koleszar, A. M., Salisbury, M. J. & Cooper, K. M. (2010). Preferential eruption of andesitic magmas through recharge filtering. *Nature Geoscience* **3**, 631–636. https://doi.org/10.1038/ngeo924.

Kent, A. J. R., Till, C. B. & Cooper, K. M. (2023). Start me up: the relationship between volcanic eruption characteristics and eruption initiation mechanisms. *Volcanica* **6**, 161–172. https://doi.org/10.30909/vol.06.02.161172.

Kiss, B., Harangi, S., Ntaflos, T., Mason, P. R. D. & Pál-Molnár, E. (2014). Amphibole perspective to unravel pre-eruptive processes and conditions in volcanic plumbing systems beneath intermediate arc volcanoes: A case study from Ciomadul volcano (SE Carpathians). *Contributions to Mineralogy and Petrology* **167**, 1–27.

Kuno, H. (1950). Petrology of Hakone volcano and the adjacent areas, Japan. *Geological Society of America Bulletin* **61**, 957–1020. https://doi.org/10.1130/0016-7606(1950)61[957:POHVAT]2.0.CO;2.

Kuo, L. C. & Kirkpatrick, R. J. (1982). Pre-eruption history of phyric basalts from DSDP legs 45 and 46: evidence from morphology and zoning patterns in plagioclase. *Contributions to Mineralogy and Petrology* **79**, 13–27. https://doi.org/10.1007/BF00376957.

Landi, P., Métrich, N., Bertagnini, A. & Rosi, M. (2004). Dynamics of magma mixing and degassing recorded in plagioclase at Stromboli (Aeolian Archipelago, Italy). *Contributions to Mineralogy and Petrology* **147**, 213–227. https://doi.org/10.1007/s00410-004-0555-5.

Laumonier, M., Scaillet, B., Pichavant, M., Champallier, R., Andujar, J. & Arbaret, L. (2014). On the conditions of magma mixing and its bearing on andesite production in the crust. *Nature Communications* **5**, 5607–5612. https://doi.org/10.1038/ncomms6607.

Leake, B. E., Woolley, A. R., Arps, C. E. S., Birch, W. D., Gilbert, M. C., Grice, J. D., Hawthorne, E., Kato, A., Kisch, H. J., Krivovichev, V. G., Linthout, K., Laird, J., Mandarino, J., Maresch, W. V., Nickel, E. H., Rock, N. M. S., Schumacher, J. C., Smith, D. C., Stephenson, N. C. N., Ungaretti, L., Whittaker, E. J. W. & Youzhi, G. (1997). Nomenclature of amphiboles: report of the subcommittee on amphiboles of the International Mineralogical Association Commission on new minerals and mineral names. *European Journal of Mineralogy* **9**, 623–651. https://doi.org/10.1127/ejm/9/3/0623.

LeBas, M. J., Le Maitre, R. W., Streckeisen, A. & Zanettin, B. (1986). A chemical classification of volcanic rocks based on the total alkali-silica diagram. *Journal of Petrology* **27**, 745–750.

Legros, F. (1998) *Téphrostratigraphie du Volcan Misti (Pérou) et Modélisation des Coulées Pyroclastiques* [Ph.D. thesis]. Clermont-Ferrand, France: Université de Blaise Pascal (Clermont-Ferrand II), p.139.

Legros, F. (2001). Tephra stratigraphy of Misti volcano, Peru. *Journal of South American Earth Sciences* **14**, 15–29. https://doi.org/10.1016/S0895-9811(00)00062-6.

Lubbers, J., Kent, A. & Russo, C. (2021). LaserTRAM-DB: a time resolved analysis module for the complete reduction of laser ablation inductively coupled plasma mass spectrometry data. *Earth ArXiv*, 1–13. https://doi.org/10.31223/X5QG95.

Lubbers, J., Kent, A. & de Silva, S. (2022). Thermal budgets of magma storage constrained by diffusion chronometry: the Cerro Galán ignimbrite. *Journal of Petrology* **63**, 1–19. https://doi.org/10.1093/petrology/egac048.

Manrique, N., Samaniego, P., Médard, E., Schiavi, F., Mariño, J. & Liorzou, C. (2020). Pre-eruptive magmatic processes associated with the historical (218 ± 14 aBP) explosive eruption of Tutupaca volcano (southern Peru). *Bulletin of Volcanology* **82**, 1–25. https://doi.org/10.1007/s00445-019-1335-4.

Mariño, J. *et al.* (2007) *Mapa de Peligros del Volcán Misti*. Instituto Geológico Minero y Metalúrgico del Perú. https://hdl.handle.net/20.500.12544/3612.

Mariño, J., Rivera, M., Thouret, J.-C. & Macedo, L. (2016). Geología y mapa de Peligros del volcán Misti. *INGEMMET Boletín Serie C: Geodinámica e Ingeniería Geológica N° 60*. https://hdl.handle.net/20.500.12544/310M.

Matthews, S. J., Sparks, R. S. J. & Gardeweg, M. C. (1999). the Piedras Grandes-Soncor eruptions, Lascar volcano, Chile; evolution of a zoned magma chamber in the Central Andean upper crust. *Journal of Petrology* **40**, 1891–1919. https://doi.org/10.1093/petroj/40.12.1891.

Morgavi, D., Laumonier, M., Petrelli, M. & Dingwell, D. B. (2022). Decrypting Magma Mixing in Igneous Systems. *Reviews in Mineralogy & Geochemistry* **87**, 607–638.

Moussallam, Y., Peters, N., Masias, P., Apaza, F., Barnie, T., Ian Schipper, C., Curtis, A., Tamburello, G., Aiuppa, A., Bani, P., Giudice, G., Pieri, D., Davies, A. G. & Oppenheimer, C. (2017). Magmatic gas percolation through the old lava dome of El Misti volcano.

Bulletin of Volcanology **79**, 1–11. https://doi.org/10.1007/s00445-017-1129-5.

Mutch, E. J. F., Maclennan, J. & Madden-Nadeau, A. L. (2022). The dichotomous nature of Mg partitioning between plagioclase and melt: Implications for diffusion chronometry. *Geochimica et Cosmochimica Acta* **339**, 173–189.

Nelson, S. T. & Montana, A. (1992). Sieve-textured plagioclase in volcanic rocks produced by rapid decompression. *American Mineralogist* **77**, 1242–1249.

Putirka, K. D. (2008). Thermometers and barometers for volcanic systems. *Reviews in Mineralogy and Geochemistry* **69**, 61–120. https://doi.org/10.2138/rmg.2008.69.3.

Putirka, K. D. (2016). Amphibole thermometers and barometers for igneous systems and some implications for eruption mechanisms of felsic magmas at arc volcanoes. *American Mineralogist* **101**, 841–858. https://doi.org/10.2138/am-2016-5506.

Reubi, O. & Blundy, J. (2009). A dearth of intermediate melts at subduction zone volcanoes and the petrogenesis of arc andesites. *Nature* **461**, 1269–1273. https://doi.org/10.1038/nature08510.

Ridolfi, F. (2021). Amp-TB2: an updated model for calcic amphibole thermobarometry. *Minerals* **11**, 1–9. https://doi.org/10.3390/min11030324.

Ridolfi, F. & Renzulli, A. (2012). Calcic amphiboles in calc-alkaline and alkaline magmas: thermobarometric and chemometric empirical equations valid up to 1,130°C and 2.2 GPa. *Contributions to Mineralogy and Petrology* **163**, 877–895. https://doi.org/10.1007/s00410-011-0704-6.

Rivera, M., Thouret, J.-C., Samaniego, P. & Le Pennec, J. L. (2014). the 2006–2009 activity of the Ubinas volcano (Peru): petrology of the 2006 eruptive products and insights into genesis of andesite magmas, magma recharge and plumbing system. *Journal of Volcanology and Geothermal Research* **270**, 122–141. https://doi.org/10.1016/j.jvolgeores.2013.11.010.

Rivera, M., Martin, H., Le Pennec, J. L., Thouret, J.-C., Gourgaud, A. & Gerbe, M. C. (2017). Petro-geochemical constraints on the source and evolution of magmas at El Misti volcano (Peru). *Lithos* **268-271**, 240–259. https://doi.org/10.1016/j.lithos.2016.11.009.

Rivera, M., Samaniego, P., Nauret, F., Mariño, J. & Liorzou, C. (2023). Petrological and geochemical constraints on the magmatic evolution at the Ampato-Sabancaya compound volcano (Peru). *Lithos* **458-459**, 107364–107320. https://doi.org/10.1016/j.lithos.2023.107364.

Ruprecht, P. & Wörner, G. (2007). Variable regimes in magma systems documented in plagioclase zoning patterns: El Misti stratovolcano and Andahua monogenetic cones. *Journal of Volcanology and Geothermal Research* **165**, 142–162. https://doi.org/10.1016/j.jvolgeores.2007.06.002.

Ruprecht, P., Bergantz, G. W., Cooper, K. M. & Hildreth, W. (2012). the crustal magma storage system of Volcán Quizapu, Chile, and the effects of magma mixing on magma diversity. *Journal of Petrology* **53**, 801–840. https://doi.org/10.1093/petrology/egs002.

Rutherford, M. J. & Devine, J. D. (2003). Magmatic conditions and magma ascent as indicated by hornblende phase equilibria and reactions in the 1995–2002 Soufriere Hills magma. *Journal of Petrology* **44**, 1433–1453. https://doi.org/10.1093/petrology/44.8.1433.

Rutherford, M. J. & Hill, P. M. (1993). Magma ascent rates from amphibole breakdown: an experimental study applied to the 1980-1986 Mount St. Helens eruptions. *Journal of Geophysical Research* **98**, 19667–19685. https://doi.org/10.1029/93JB01613.

Ryan, J., Beck, S., Zandt, G., Wagner, L., Minaya, E. & Tavera, H. (2016). Central Andean crustal structure from receiver function analysis. *Tectonophysics* **682**, 120–133. https://doi.org/10.1016/j.tecto.2016.04.048.

Samaniego, P., Rivera, M., Manrique, N., Schiavi, F., Nauret, F., Liorzou, C. & Ancellin, M. A. (2020). Linking magmatic processes and magma chemistry during the post-glacial to recent explosive eruptions of Ubinas volcano (southern Peru). *Journal of Volcanology and Geothermal Research* **407**, 107095–107025. https://doi.org/10.1016/j.jvolgeores.2020.107095.

Schmidt, M. W. (1992). Amphibole composition in tonalite as a function of pressure: an experimental calibration of the Al-in-hornblende barometer. *Contributions to Mineralogy and Petrology* **110**, 304–310. https://doi.org/10.1007/BF00310745.

Seaman, S. J. (2000). Crystal clusters, feldspar glomerocrysts, and magma envelopes in the Atascosa Lookout lava flow, Southern Arizona, USA: recorders of magmatic events. *Journal of Petrology* **41**, 693–716. https://doi.org/10.1093/petrology/41.5.693.

Siebert, L., Simkin, T. & Kimberly, P. (2011) *Volcanoes of the World*. University of California Press, Berkeley.

de Silva, S. & Francis, P. W. (1991). Potentially active volcanoes of Peru—observations using Landsat Thematic Mapper and Space Shuttle imagery. *Bulletin of Volcanology* **52**, 286–301. https://doi.org/10.1007/BF00304100.

de Silva, S., Salas, G. & Schubring, S. (2008). Triggering explosive eruptions—the case for silicic magma recharge at Huaynaputina, southern Peru. *Geology* **36**, 387–390. https://doi.org/10.1130/G24380A.1.

Singer, B. S., Dungan, M. A. & Layne, G. D. (1995). Textures and Sr, Ba, Mg, Fe, K, and Ti compositional profiles in volcanic plagioclase: clues to the dynamics of calc-alkaline magma chambers. *American Mineralogist* **80**, 776–798. https://doi.org/10.2138/am-1995-7-815.

Sparks, R. S. J. & Marshall, L. A. (1986). Thermal and mechanical constraints on mixing between mafic and silicic magmas. *Journal of Volcanology and Geothermal Research* **29**, 99–124. https://doi.org/10.1016/0377-0273(86)90041-7.

Sparks, S. R. J., Sigurdsson, H. & Wilson, L. (1977). Magma mixing: a mechanism for triggering acid explosive eruptions. *Nature* **267**, 315–318. https://doi.org/10.1038/267315a0.

Spear, F. (1981). An experimental study of hornblende stability and compositional variability in amphibolite. *American Journal of Science* **281**, 697–734. https://doi.org/10.2475/ajs.281.6.697.

Takach, M. K., Tepley, F. J., Harpel, C. J., Aguilar, R. & Rivera, M. (2021). Deciphering the petrology of a hazardous volcano: magma storage conditions, remobilization, and timescales inferred from tephra-fall deposits from Misti volcano, Peru. *Geological Society of America Abstracts with Programs* **53**. https://doi.org/10.1130/abs/2021AM-368132.

Takach, M. K., Tepley, F. J., Harpel, C. J., Aguilar, R. & Rivera, M. (2022). Unraveling magma recharge and storage histories with geochemistry, crystal populations, and thermobarometry in the Pacheco sequence of Misti volcano, Peru. *Geological Society of America Abstracts with Programs* **54**. https://doi.org/10.1130/abs/2022AM-382784.

Takach, M. K., Tepley, F. J., Harpel, C. J., Aguilar, R. & Rivera, M. (2024) *Geochemical data for the Pacheco stage tephra-fall deposits from Misti volcano*. Arequipa, Peru: U.S. Geological Survey data release.

Tepley, F. J., Davidson, J. P. & Clynne, M. A. (1999). Magmatic interactions as recorded in plagioclase phenocrysts of Chaos Crags, Lassen Volcanic Center, California. *Journal of Petrology* **40**, 787–806. https://doi.org/10.1093/petroj/40.5.787.

Tepley, F. J., Davidson, J. P., Tilling, R. I. & Arth, J. G. (2000). Magma mixing, recharge and eruption histories recorded in plagioclase phenocrysts from El Chichón Volcano, Mexico. *Journal of Petrology* **41**, 1397–1411.

Tepley, F. J., De Silva, S. & Salas, G. (2013). Magma dynamics and petrological evolution leading to the VEI 5 2000 BP eruption of El Misti volcano, southern Peru. *Journal of Petrology* **54**, 2033–2065. https://doi.org/10.1093/petrology/egt040.

Thomas, W. M. & Ernst, W. G. (1990) The aluminum content of hornblende in calc-alkaline granitic rocks: A mineralogic barometer calibrated experimentally to 12 kbars. In: Spencer R. J. & Chou I.-M. (eds) *Fluid-Mineral Interactions*. The Geochemical Society, 59–63.

Thouret, J.-C., Legros, F., Gourgaud, A., Salas, G., Juvigné, E., Gilot, E., Uribe, M. & Rodriguez, A. (1995). Un example de prévision des risques vol- caniques au Pérou méridional (région d'Arequipa), fondé Sur l'étude de l'activité éruptive récente du strato-volcan El Misti: Comptes Rendus de l'Académie des Sciences, ser. *II, Sciences de la Terre et des Planètes* **320**, 923–929.

Thouret, J.-C., Davila, J. & Eissen, J. P. (1999). Largest explosive eruption in historical times in the Andes at Huaynaputina volcano, A.D. 1600, southern Peru. *Geology* **27**, 435–438. https://doi.org/10.1130/0091-7613(1999)027<0435:LEEIHT>2.3.CO;2.

Thouret, J.-C., Finizola, A., Fornari, M., Legeley-Padovani, A., Suni, J. & Frechen, M. (2001). Geology of El Misti volcano near the city of Arequipa, Peru. *Geological Society of America Bulletin* **113**, 1593–1610. https://doi.org/10.1130/0016-7606(2001)113<1593:GOEMVN>2.0.CO;2.

Tsuchiyama, A. (1985). Dissolution kinetics of plagioclase in the melt of the system diopside–albite–anorthite, and origin of dusty plagioclase in andesites. *Contributions to Mineralogy and Petrology* **89**, 1–16. https://doi.org/10.1007/BF01177585.

Venezky, D. Y. & Rutherford, M. J. (1997). Preeruption conditions and timing of dacite–andesite magma mixing in the 2.2 ka eruption at Mount Rainier. *Journal of Geophysical Research* **102**, 20069–20086. https://doi.org/10.1029/97JB01590.

Venezky, D. Y. & Rutherford, M. J. (1999). Petrology and Fe-Ti oxide reequilibration of the 1991 Mount Unzen mixed magma. *Journal of Volcanology and Geothermal Research* **89**, 213–230. https://doi.org/10.1016/S0377-0273(98)00133-4.

Vlastelic, I., Apaza, F., Masias, P., Rivera, M., Piro, J. L. & Gannoun, A. (2022). Probing the hidden magmatic evolution of El Misti volcano (Peru) with the Pb isotope composition of fumaroles. *Bulletin of Volcanology* **84**, 1–12. https://doi.org/10.1007/s00445-021-01521-9.

Walker, B. A., Klemetti, E. W., Grunder, A. L., Dilles, J. H., Tepley, F. J. & Giles, D. (2013). Crystal reaming during the assembly, maturation, and waning of an eleven-million-year crustal magma cycle: Thermobarometry of the Aucanquilcha Volcanic Cluster. *Contributions to Mineralogy and Petrology* **165**, 663–682.

Wang, X., Hou, T., Wang, M., Zhang, C., Zhang, Z., Pan, R., Marxer, F. & Zhang, H. (2021). A new clinopyroxene thermobarometer for mafic to intermediate magmatic systems. *European Journal of Mineralogy* **33**, 621–637. https://doi.org/10.5194/ejm-33-621-2021.

Wieser, P., Petrelli, M., Lubbers, J., Wieser, E., Ozaydin, S., Kent, A. & Till, C. (2022). Thermobar: an open-source Python3 tool for thermobarometry and hygrometry. *Volcanica* **5**, 349–384. https://doi.org/10.30909/vol.05.02.349384.

Wilcox, R. (1999). The idea of magma mixing: history of a struggle for acceptance. *Journal of Geology* **107**, 421–432. https://doi.org/10.1086/314357.

Wörner, G., Mamani, M. & Blum-Oeste, M. (2018). Magmatism in the Central Andes. *Elements* **14**, 237–244. https://doi.org/10.2138/gselements.14.4.237.